

Spectra of Black Hole Accretion Models of Ultra-Luminous X-ray Sources

Ramesh Narayan^{1*}, Aleksander Sądowski^{2*}, Roberto Soria^{3,4*}

¹*Harvard-Smithsonian Center for Astrophysics, 60 Garden Street, Cambridge, MA 02138, USA*

²*MIT Kavli Institute for Astrophysics and Space Research, 77 Massachusetts Ave, Cambridge, MA 02139, USA*

³*International Centre for Radio Astronomy Research, Curtin University, GPO Box U1987, Perth, WA 6845, Australia*

⁴*Sydney Institute for Astronomy, School of Physics A28, The University of Sydney, NSW 2006, Australia*

7 February 2017

ABSTRACT

We present general relativistic radiation MHD simulations of super-Eddington accretion on a $10M_{\odot}$ black hole. We consider a range of mass accretion rates, black hole spins, and magnetic field configurations. We compute the spectra and images of the models as a function of viewing angle, and compare them with the observed properties of ultraluminous X-ray sources (ULXs). The models easily produce apparent luminosities in excess of 10^{40} erg s⁻¹ for pole-on observers. However, the angle-integrated radiative luminosities rarely exceed 2.5×10^{39} erg s⁻¹ even for mass accretion rates of tens of Eddington. The systems are thus radiatively inefficient, though they are energetically efficient when the energy output in winds and jets is also counted. The simulated models reproduce the main empirical types of spectra — disk-like, super-soft, soft, hard — observed in ULXs. The magnetic field configuration, whether MAD (“magnetically arrested disk”) or SANE (“standard and normal evolution”), has a strong effect on the results. In SANE models, the X-ray spectral hardness is almost independent of accretion rate, but decreases steeply with increasing inclination. MAD models with non-spinning black holes produce significantly softer spectra at higher values of \dot{M} , even at low inclinations. MAD models with rapidly spinning black holes are quite different from all other models. They are radiatively efficient (efficiency factor $\sim 10 - 20\%$), super-efficient when the mechanical energy output is also included (70%), and produce hard blazar-like spectra. In all models, the emission shows strong geometrical beaming, which disagrees with the more isotropic illumination favoured by observations of ULX bubbles.

Key words: methods: numerical – radiative transfer – accretion, accretion discs – black hole physics – X-rays: binaries

1 INTRODUCTION

Ultraluminous X-ray sources (ULXs) are a class of highly luminous, compact, non-nuclear X-ray sources in nearby spiral galaxies, whose luminosities exceed the Eddington luminosity limit of a neutron star, or even that of a $10M_{\odot}$ black hole (Fabbiano 1989; Makishima et al. 2000; Swartz et al. 2004). The nature of these mysterious sources is still not understood.

Because of their very large apparent luminosities — few $\times 10^{39}$ erg s⁻¹ to above 10^{40} erg s⁻¹ in a few cases — it was suggested that ULXs might be intermediate mass

black holes (BHs) (Miller & Colbert 2004). While one or two ULXs may well be intermediate mass BHs (e.g., HLX-1: Farrell et al. 2009; Godet et al. 2009; Davis et al. 2011), the more recent consensus (see Bachetti 2016; Feng & Soria 2011 for reviews, and King et al. 2001; Begelman et al. 2006; Poutanen et al. 2007 for theoretical arguments) is that the vast majority of ULXs are stellar-mass ($\sim 10M_{\odot}$) BHs, accreting above their Eddington limit. But not all ULXs are BHs: three objects show coherent pulsations and are thus neutron stars (Bachetti et al. 2014; Israel et al. 2017, 2016; Fürst et al. 2017, 2016). It is unclear what fraction of ULXs belong to this class (King & Lasota 2016).

The identification of accreting neutron stars within the ULX population implies that accreting systems can certainly have highly super-Eddington apparent luminosities. Two al-

* E-mail: rnarayan@cfa.harvard.edu; asadowsk@mit.edu; Roberto.Soria@curtin.edu.au

ternative physical scenarios might explain this fact. One possibility is that the photon emission of super-critical neutron stars and black holes is strongly collimated along the polar axis, and appears highly super-Eddington only for observers located in that direction; a beaming factor scaling as $(\dot{M}/\dot{M}_{\text{Edd}})^2$ was proposed by King (2009). Another scenario (Israel et al. 2016), specific to neutron stars, is that the classical Eddington limit is not a barrier to accretion onto a highly magnetized neutron star because the electron scattering cross section (and therefore the effect of radiation pressure) is reduced for photon energies in the X-ray band, in the presence of a magnetic field $B \gtrsim 10^{12}$ G (Herold 1979).

Regardless of details, an unavoidable consequence of super-critical accretion is that the inflow cannot settle into a standard, radiatively efficient, optically thick, geometrically thin accretion disk (Shakura & Sunyaev 1973). A generalization of the thin disk, the “slim disk” model (Abramowicz et al. 1988) has been widely applied to the regime of super-Eddington accretion, including ULXs (e.g., Watarai et al. 2001). It is a useful first approximation in the study of such objects. However, these idealized analytic models are not appropriate for detailed comparison with observations, as it is generally believed that super-Eddington flows will have massive radiatively-driven outflows. Such outflows are intrinsically two-dimensional and cannot be understood within a height-integrated 1D accretion framework. The winds will cause anisotropic emission, with geometric collimation of the radiation along the polar axis. The gas in the wind will also scatter the radiation from the disk. Predicting the spectral appearance and apparent luminosity of a super-critical accretor, as seen by distant observers, is therefore a challenging problem that requires numerical simulations.

Pioneering work on simulating super-Eddington accretion disks was done by Ohsuga and collaborators, who developed radiation-hydrodynamic (Ohsuga et al. 2005) and radiation-MHD codes (Ohsuga & Mineshige 2011). Using an axisymmetric two-dimensional model with a pseudo-Newtonian potential (Paczyński & Wiita 1980), Kawashima et al. (2012) calculated the apparent luminosity and spectral appearance of super-Eddington sources for different viewing angles; their calculations included bulk and thermal Compton upscattering of seed disk photons in a hot (shocked) inner region, and Compton downscattering and absorption through a dense outflow. The authors obtained good agreement between their model predictions and spectra observed in some ULXs.

During the last few years, fully general relativistic radiation MHD codes have been developed by a number of groups (Sądowski et al. 2013, 2014; McKinney et al. 2014; Fragile et al. 2014; Takahashi & Ohsuga 2015; Takahashi et al. 2016). In this paper, we use one of these state-of-the-art codes, KORAL (Sądowski et al. 2013, 2014), to explore the super-Eddington accreting stellar-mass BH model of ULXs. We present a number of general relativistic radiation MHD simulations of accreting BHs, corresponding to a range of super-Eddington mass accretion rates, BH spins and magnetic field strengths. We compute spectra and images corresponding to these simulations using a radiative-transfer and ray-tracing code HEROIC (Narayan et al. 2016; Zhu et al.

2015). We then discuss to what extent the numerical accretion models reproduce the observed spectra of ULXs.

While ULXs are of great interest in and of themselves, they are also convenient prototypes of super-Eddington accretion flows in other more distant objects. It is believed that many tidal disruption events (TDEs) go through a super-Eddington phase at early times (Alexander et al. 2016; Socrates 2012; Lodato & Rossi 2011; Rees 1988; Zauderer et al. 2011). A sub-class of active galactic nuclei (AGN) in the local universe, known as Narrow Line Seyfert 1 galaxies, are likely close to the Eddington limit and in some cases probably super-Eddington (Jin et al. 2016; Castelló-Mor et al. 2016; Zubovas & King 2013; Kawakatu & Ohsuga 2011; Collin & Kawaguchi 2004). Finally, the rapid early growth of supermassive BHs, as evidenced by the presence of very massive BHs at high redshifts (Wu et al. 2015; Zuo et al. 2015; Mortlock et al. 2011), and also from direct measurements of the luminosity from the most powerful quasars (Wang et al. 2015; Page et al. 2014; Kelly & Shen 2013), might indicate that these BHs grew via a super-Eddington phase in the early universe (Lupi et al. 2016; Volonteri et al. 2015; Volonteri & Rees 2005; Madau et al. 2014; King 2003). Progress in these fields will be possible only when we develop tools for studying super-Eddington accretion and understand the nature of such flows.

Longstanding questions on the nature of super-Eddington accretion include: (i) How viable is super-Eddington accretion in the first place? (We now know that it is certainly viable because some ULXs have turned out to be accreting neutron stars.) (ii) What is the geometry of the accretion flow? How does it impact observations as a function of inclination angle? (iii) How luminous are super-Eddington systems? Are they radiatively efficient? (iv) How much mechanical energy do super-Eddington disks produce in outflows? What role do the outflows play in feedback? (v) How often do super-Eddington disks produce relativistic jets? How do these jets compare with blazar jets?

ULXs have several advantages for exploring these basic questions. Even though we do not have a precise BH mass measurement for any individual ULX, it is reasonable to assume that the mass of a typical ULX (the non-neutron star variety) is not very different from $\sim 10M_{\odot}$ (by no more than a factor of 2-3). This eliminates one large source of uncertainty. ULXs exhibit at least four different spectral states, which indicates that the complex physics of super-Eddington accretion is well-represented by this population. In a few sources, transitions between spectral states have been observed, which is likely to be helpful for understanding the origin of the different states. ULXs have bubbles of ionized gas surrounding them, which provide information on the net angle-integrated outflow of radiation and mechanical energy from the accreting BH. This gives independent constraints on the isotropic energy output of the system, as distinct from any geometrically focused radiation that may be received directly from the accretion disk. The present study represents a first effort at understanding these and other observations of ULXs.

In §2, we describe the numerical methods used in this work, specifically, the general relativistic radiation MHD (GRRMHD) code KORAL and the radiation post-processing code HEROIC. In §3, we discuss results for our fiducial model, which consists of a $10M_{\odot}$ non-spinning BH, accreting at 10

times the Eddington mass accretion rate. In §4, we carry out a parameter study, where we compare models with different mass accretion rates, BH spins, and magnetic field strengths. In §5, we compare the simulation results and computed spectra with observations of ULXs. The comparison is promising, but there are also clear discrepancies. Finally, in §6, we conclude with a summary and discussion.

2 NUMERICAL METHODS

The computations discussed in this paper are done in three stages, as described in the following subsections. First, we run a GRRMHD simulation of the accretion flow for the chosen model parameters. Next, we transfer the simulation output to a second grid and extrapolate the data to large radii, where the GRRMHD data have not converged. Finally, we solve for the radiation field on the second grid using a post-processing code

2.1 GRRMHD simulations with KORAL

The simulations were done using the GRRMHD code KORAL (Sądowski et al. 2013, 2014), which evolves gas, magnetic field and radiation in a fixed gravitational metric. In the present work, we use the Kerr metric in Kerr-Schild coordinates. The magnetic field is evolved assuming ideal MHD (no resistivity) and the radiation is described by means of frequency-integrated angular moments, with the moment expansion closed via the M1 closure method (Levermore 1984). A radiative viscosity term is included in order to mitigate some of the limitations of the M1 scheme (Sądowski et al. 2015).

The radiative processes included in the present simulations are free-free emission and absorption, and Compton scattering, where the latter is handled via a photon-conserving scheme (Sądowski & Narayan 2015a). KORAL and its sister code HARMRAD (McKinney et al. 2014) are capable of modeling additional radiation processes such as thermal synchrotron (Sądowski et al. 2016a) and double Compton (McKinney et al. 2016), but these were not included in the present work.

Table 1 lists the key parameters of the 13 simulations discussed in this paper. All models assume a BH mass $M = 10M_{\odot}$. Of the 13 simulations, 6 have been done in 3D, where the magnetorotational instability (MRI, Balbus & Hawley 1991, 1998) is well-resolved and develops robustly, while 7 are in 2D. It is well-known that the MRI cannot be sustained in 2D, so 2D MHD simulations cannot achieve steady state accretion. To overcome this problem, we employ the mean-field magnetic dynamo prescription described in Sądowski et al. (2015), which permits us to run 2D simulations for arbitrarily long times. Previous tests have shown that such 2D simulations agree well with their 3D counterparts, at least in their time-averaged properties (Sądowski & Narayan 2015b), and are an economical way of running simulations.

All simulations were initialized with an equilibrium torus of weakly magnetized gas orbiting the BH. The torus parameters are chosen to correspond closely to the initial setup of earlier simulations described in Sądowski & Narayan (2016). The initial gas density in the torus is adjusted to obtain the desired mass accretion rate. The topol-

Table 1. List of simulated models

Model	$\dot{M}/\dot{M}_{\text{Edd}}$	a_*	Field Strength	2D/3D
r010_3d	10	0	SANE	3D
r010_2d	10	0	SANE	2D
r012_3d	1.2	0	SANE	3D
r030_2d	7.0	0	SANE	2D
r031_2d	17	0	SANE	2D
r011_2d	12	0.9	SANE	2D
r032_2d	6.2	0.9	SANE	2D
r033_2d	10	0.9	SANE	2D
r034_2d	26	0.9	SANE	2D
r013_3d	23	0	MAD	3D
r023_3d	1.3	0	MAD	3D
r014_3d	36	0.9	MAD	3D
r015_3d	6.8	0.9	MAD	3D

ogy of the initial seed magnetic field is also adjusted, depending on the requirements. In the case of MAD (“Magnetically Arrested Disk”, Igumenshchev et al. 2003; Narayan et al. 2003; Tchekhovskoy et al. 2011) models, we initialize the simulation with a single large-scale loop, while for SANE (“Standard and Normal Evolution”, Narayan et al. 2012) models, we use multiple loops of alternating polarity.

The 2D simulations were run with a resolution of 320×320 cells in r - θ , and the 3D runs with a resolution of $320 \times 320 \times 32$, with 32 cells in azimuth spanning a $\pi/2$ wedge, with periodic boundary conditions. The adopted grid is logarithmic in r and slightly biased towards the equatorial plane in θ . Every simulation is run until a final time of $25,000 GM/c^3$, which in most cases gives a well converged solution extending up to $r \sim 30 GM/c^2$ at the equatorial plane, and much farther out at higher latitude.

The 3D model r010_3d, shown in bold in the first line of Table 1, is our *fiducial* model. It considers a non-spinning BH, $a_* \equiv a/M = 0$, and has a mass accretion rate $\dot{M} = 10\dot{M}_{\text{Edd}}$. In this paper, we define \dot{M}_{Edd} in terms of the Eddington luminosity, $L_{\text{Edd}} = 1.25 \times 10^{38} (M/M_{\odot}) \text{ erg s}^{-1}$, for the given BH mass M ,

$$\dot{M}_{\text{Edd}} = \frac{L_{\text{Edd}}}{\eta_{\text{NT}} c^2}, \quad (1)$$

where η_{NT} is the radiative efficiency of the Novikov & Thorne (1973) general relativistic thin accretion disk model. For $a_* = 0$, $\eta_{\text{NT}} = 0.05719$, while for $a_* = 0.9$ (below), $\eta_{\text{NT}} = 0.1558$. The fiducial model is initialized with a weak poloidal magnetic field in multiple loops such that, even after the disk has reached steady state for a considerable period of time, the poloidal field strength at the BH horizon is still at the SANE level.

Model r010_2d is identical to the fiducial model, but it is run in 2D. This model is used to verify that results in 2D are close to those obtained in 3D.

Models r012_3d, r030_2d and r031_2d are similar to the previous two models in that they have $a_* = 0$ and a SANE magnetic field, but their mass accretion rates are different, as indicated in Table 1.

Models r011_2d, r032_2d, r033_2d and r034_2d correspond to spinning BHs, with $a_* = 0.9$. These models cover a range of values of \dot{M} , and all have SANE magnetic fields.

The final 4 models in Table 1 were initialized with a single poloidal loop of magnetic field and therefore ended

up with strong poloidal magnetic fields, corresponding to the MAD limit. Models r013.3d and r023.3d have a non-spinning BH, $a_* = 0$, while models r014.3d and r015.3d have a spinning BH, $a_* = 0.9$. All MAD models have significant non-axisymmetric structure (Igumenshchev et al. 2003; Tchekhovskoy et al. 2011; McKinney et al. 2012), and they have to be run in 3D.

2.2 Radial extrapolation of simulated models

Two steps are needed before the KORAL simulation output can be post-processed by the radiation solver described in §2.3.

First, time-averaged and azimuth-averaged (in the case of 3D simulations) data are interpolated on to the grid that will be used during the post-processing stage. We use 81 cells distributed uniformly in θ and 50 cells per decade distributed uniformly in $\log r$. This gives roughly square cells in $r\theta$, which minimizes the effects of ray defects (Zhu et al. 2015). The radial grid extends from an inner radius just outside the BH horizon to an outer radius $r_{\text{out}} = 10^5 GM/c^2$.

The KORAL data are averaged over the chosen time duration, which is the last 5,000 GM/c^3 of each simulation, and over the full azimuth range of $\pi/2$ in the case of 3D simulations. The data are then transferred to the new grid by simple linear interpolation. In the case of the viscous heating rate q^+ , we ignore the KORAL values in the four cells in θ closest to the poles, where boundary conditions make the results unreliable, and instead extrapolate from larger θ .

The second step is to cut out regions of the KORAL simulation that are outside the converged region of the simulation and to extrapolate the KORAL data to these cells. For each cell in the interpolated grid, we compute the poloidal velocity, $v_{\text{pol}} = (v_r^2 + v_\theta^2)^{1/2}$, and compute a flow time $t_{\text{flow}} = r/v_{\text{pol}}$. We then compare t_{flow} to a characteristic simulation duration t_{sim} of the KORAL simulation. For the latter, we use either $t_{\text{sim}} = 5,000 GM/c^3$, the duration over which the simulation output is time-averaged, or $t_{\text{sim}} = 12,500 GM/c^3$, half the total duration of the simulation (they give similar results).

If $t_{\text{flow}} < t_{\text{sim}}$, we consider the fluid in the cell in the KORAL simulation to have reached steady state. After identifying all the cells in the grid that are in steady state requirement, for each θ , we call the outermost radius that satisfies this condition as the limiting equilibrium radius $r_{\text{eq}}(\theta)$. Cells with $r > r_{\text{eq}}(\theta)$ have $t_{\text{flow}} > t_{\text{sim}}$ and are less likely to have achieved steady state.

The white contour in Figure 1 shows the boundary of the steady-state region, $r_{\text{eq}}(\theta)$, for the fiducial model. In the equatorial regions, steady state is achieved out to radii $\sim 30 GM/c^2$, but we arbitrarily set $r_{\text{eq}}(\theta) = 50 GM/c^2$. The KORAL simulation data are somewhat less reliable in the radius range $r/(GM/c^2) \sim 30 - 50$, but we feel it is better to use the simulation data here rather than purely extrapolated data since there is non-negligible viscous dissipation at these radii. In addition, there is non-negligible radial advection of radiation in a couple of the models, and it is hard to model advection correctly in extrapolated data. In the polar regions, because of the large velocity of outflowing gas, steady state is achieved to much larger radii. In fact, for angles within about 30° of the poles, the flow is in steady state out to the edge of the KORAL simulation at $r = 10^3 GM/c^2$. To avoid edge effects, we ignore the last 5 radial cells in the

KORAL output, so this limits $r_{\text{eq}}(\theta)$ to around $900 GM/c^2$ in the polar regions.

For cells with $r > r_{\text{eq}}(\theta)$, we extrapolate from the KORAL values at $r = r_{\text{eq}}(\theta)$, using an appropriate scaling as a function of r . In all our simulations, the accretion flow has two distinct regions: (i) An inflow region which is restricted to a range of angles around the equator, and (ii) an outflow region which consists of higher latitudes, extending up to the poles. For each quantity that we extrapolate, we first identify which of these two zones is more important to model correctly. We then choose a radial scaling appropriate for that zone, but apply it to the entire extrapolated volume. Although the scaling may be inconsistent for the other zone, it generally does not matter. With this idea in mind, the scalings we use for the extrapolated region, $r > r_{\text{eq}}(\theta)$, are as follows:

$$\rho(r, \theta) = \rho[r_{\text{eq}}(\theta)] \left[\frac{r}{r_{\text{eq}}(\theta)} \right]^{-2}, \quad (2)$$

$$v_r(r, \theta) = v_r[r_{\text{eq}}(\theta)], \quad (3)$$

$$v_\theta(r, \theta) = v_\theta[r_{\text{eq}}(\theta)] \left[\frac{r}{r_{\text{eq}}(\theta)} \right]^{-1/2}, \quad (4)$$

$$v_\phi(r, \theta) = v_\phi[r_{\text{eq}}(\theta)] \left[\frac{r}{r_{\text{eq}}(\theta)} \right]^{-1/2}, \quad (5)$$

$$T_{\text{gas}}(r, \theta) = T_{\text{gas}}[r_{\text{eq}}(\theta)] \left[\frac{r}{r_{\text{eq}}(\theta)} \right]^{-1}, \quad (6)$$

$$q^+(r, \theta) = q^+[r_{\text{eq}}(\theta)] \left[\frac{r}{r_{\text{eq}}(\theta)} \right]^{-4} \quad (\text{poles}), \quad (7)$$

$$|B|(r, \theta) = |B|[r_{\text{eq}}(\theta)] \left[\frac{r}{r_{\text{eq}}(\theta)} \right]^{-3/2}. \quad (8)$$

The scalings for ρ and v_r (eqs. 2, 3) are driven by our desire to model the outflow density and dynamics correctly. Specifically, we wish the outflowing gas to coast at a constant radial velocity (which is reasonable because r_{eq} is usually large enough that we are outside the acceleration zone of the outflow), and to conserve mass. These scalings are not accurate for the inflowing equatorial disk, but we believe that the error we make is unimportant since the gas here has a very low radial velocity and is optically thick. Figure 1 shows the density distribution we obtain via this extrapolation technique for the fiducial model.

For v_θ and v_ϕ , we use a Keplerian scaling with radius (eqs. 4, 5), as appropriate for gas orbiting in the disk. This is particularly important for v_ϕ , which can produce significant Doppler shifts even at largish radii. In the outflow region, v_θ and v_ϕ are much smaller than v_r , and it does not matter what scaling we use.

For the gas temperature T_{gas} , we use a virial argument to choose a radial scaling $\propto r^{-1}$ (eq. 6). The precise choice is not important since, in most of our radiation modeling, we solve self-consistently for the gas temperature (§2.3).

We scale the viscous heating rate q^+ ($\text{erg cm}^{-3} \text{s}^{-1}$) as r^{-4} (eq. 7). This is demanded by the requirement that $r^3 q^+$ should vary as r^{-1} , the fractional energy released down to radius r . In practice, we extrapolate only at polar angles, where the amount of heating involved is not large. In the equatorial region, we use thin disk theory to determine the amount of energy dissipated as a function of radius and angle. Specifically, we take the dissipation rate per unit area

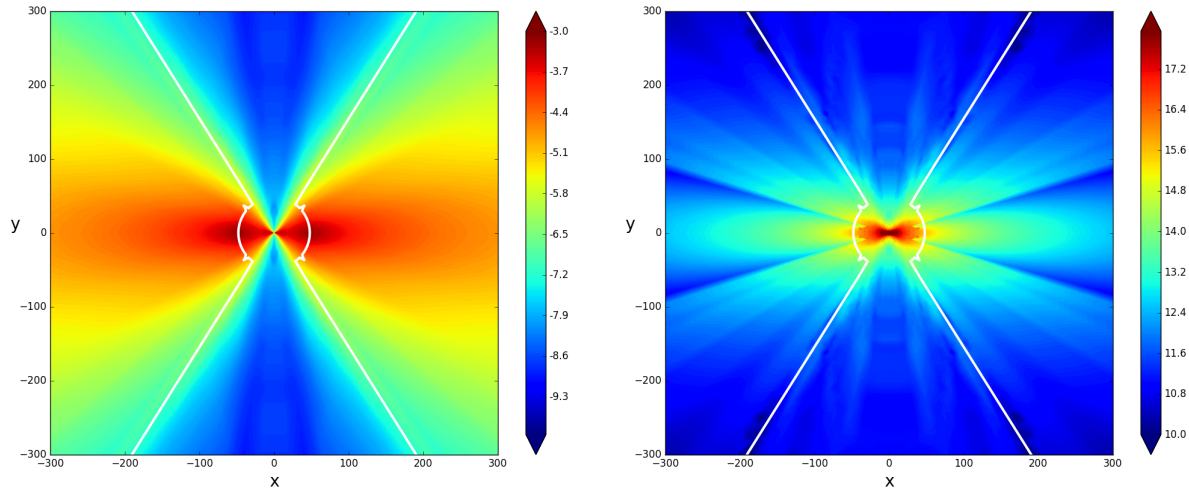


Figure 1. The two panels show the distribution of the logarithm of the density $\log \rho$ (left) and logarithm of the viscous heating rate $\log q^+$ (right) in the poloidal plane of the fiducial model r010.3d. The BH is at the center and coordinates are expressed in mass units (GM/c^2). The disk equatorial plane is oriented horizontally and the two polar funnels are oriented vertically. The regions inside the white contour are in steady state in the KORAL simulation. Outside the white contours, the KORAL data are extrapolated, as explained in §2.2.

Q^+ (erg cm^{-2}) of a non-relativistic thin disk of given M and \dot{M} (Shakura & Sunyaev 1973),

$$Q^+(r) = \frac{3GM\dot{M}}{4\pi r^3} \left[1 - \left(\frac{r}{r_{\text{in}}} \right)^{-1/2} \right], \quad (9)$$

and distribute it with a gaussian distribution in θ around the equatorial plane to model the dissipation rate per unit volume q^+ (erg cm^{-3}):

$$q^+(r, \theta) = \frac{Q^+(r)}{\sqrt{2\pi}r\theta_s} \exp \left[-\frac{(\theta - (\pi/2))^2}{2\theta_s^2} \right] \quad (\text{equator}). \quad (10)$$

We use $\theta_s = 0.1$ for the angular scale height (the exact value is unimportant since this heating occurs deep inside the optically thick portion of the disk), and $r_{\text{in}} = 6GM/c^2$ for the nominal inner edge of the thin disk model. Figure 1 shows the resulting distribution of q^+ . Note that the bulk of the viscous energy release occurs inside the steady state region $r < r_{\text{eq}}(\theta)$, where we use KORAL results, so the energy release in the extrapolated region, whether we use the polar extrapolation (7) or the equatorial extrapolation (10), is quantitatively small.

Finally, the magnetic field strength $|B|$, which is needed for one test where we include thermal synchrotron emission, is scaled as $r^{-3/2}$ (eq. 8). This is to ensure that the magnetic pressure $B^2/8\pi$ scales the same way as the gas pressure ρT_{gas} .

We extrapolate all the above quantities out to a radius $r_{\text{out}} = 10^5 GM/c^2$. This is perhaps farther out than necessary. However, we feel that there is value in allowing the radiation model to include opacity and reprocessing effects at large radii. Since our grid is logarithmic in radius, the extra cost of handling a large range of radius during the radiation post-processing step is not excessive.

2.3 Radiation post-processing with HEROIC

Radiation post-processing is done using the multi-dimensional, general relativistic code HEROIC (Narayan et al. 2016; Zhu et al. 2015). This code takes the density, velocity, viscous dissipation rate and other quantities in the interpolated grid described in §2.2, and solves in detail for the radiation field in each grid cell. In the present work, we describe the angular distribution of the radiation field by solving for the intensity on 162 angles distributed uniformly over the sphere in the local fluid frame of each cell. We use 101 frequencies, distributed uniformly in $\log \nu$ from $\nu = 10^{14} - 10^{24}$ Hz, to describe the radiation spectrum of each angular ray in each spatial cell.

A number of enhancements have been made to HEROIC since publication of the original methods papers (Zhu et al. 2015; Narayan et al. 2016). In brief:

(i) The treatment of bremsstrahlung in the relativistic regime has been improved. The emissivity at relativistic temperatures now uses the formulae given in Narayan & Yi (1995); the corresponding spectral distribution follows the prescriptions in Gould (1980).

(ii) For temperatures below 10^8 K, the code uses an opacity table corresponding to solar abundances taken from the CHIANTI database (Dere et al. 1997; Landi et al. 2013; Del Zanna et al. 2015); the opacity includes both bound-free and free-free contributions. However, for simplicity, we assume that the spectral distribution is the same as for free-free (i.e., we ignore features like atomic edges).

(iii) The previous Comptonization routine in HEROIC (Narayan et al. 2016), which was based on solving the Kompaneets equation, has been supplemented with a relativistic module for temperatures above $10^{8.5}$ K; this module uses the Comptonization kernel of Jones (1968), with the corrections given in Coppi & Blandford (1990).

(iv) Thermal synchrotron emission and absorption are in-

cluded, using the approximate formulae given in Narayan & Yi (1995) and Mahadevan et al. (1996); this feature is used only in one test in this paper.

(v) The code can handle two-temperature plasmas, including the effects of advection, as required for simulation output from the recently-developed two-temperature version of KORAL (Sądowski et al. 2016b); this improvement is not needed for the present work.

(vi) Finally, the code now works with both short and long characteristics (see Zhu et al. 2015).

The radiative post-processing is done using the interpolated and extrapolated data described in §2.2. The computations consist of a number of stages, as described below:

Stage I: First, we keep the gas temperature T_{gas} fixed at the values described in §2.2, and we iteratively solve for the radiation field (all angles, all frequencies, all cells), using the radiative transfer equation and the method of short characteristics (Zhu et al. 2015; Narayan et al. 2016).

Stage II: Next, we relax the constraint on the gas temperature, and solve simultaneously for both the temperature and the radiation field, again using short characteristics. In this stage, we use the viscous heating rate q_+ as a constraint and apply the condition of energy balance (Narayan et al. 2016) to solve for the temperature. This step is necessary because the KORAL radiation model is fairly crude (just a few frequency-integrated angular moments), so the KORAL temperatures are not reliable. The viscous dissipation on the other hand is likely to be more robust since it ultimately comes from energy conservation, which KORAL satisfies well.

Stage III: Next, we take the solution from the second stage and improve it with around 10 iterations of long characteristics, again solving for both the temperature and the radiation field.

Stage IV: Finally, we take the output from the third stage and carry out ray-tracing to calculate the observed spectrum and/or image for observers located at various orientations with respect to the disk.

All of the radiation physics and ray-tracing in HEROIC is done using general relativistic photon geodesics, including ray deflections, Doppler shifts and gravitational redshift. Even though the interpolated grid described in §2.2 is in 2D (r - θ), the radiative transfer calculations are done in 3D, assuming axisymmetry.¹

3 FIDUCIAL MODEL

3.1 Comparing KORAL and HEROIC

We discuss here in some detail the fiducial model, r010_3d, which has a BH with $M = 10M_{\odot}$ and $a_* = 0$. The mass accretion rate is $\dot{M} = 10\dot{M}_{\text{Edd}}$, and the magnetic field strength corresponds to the SANE regime.

KORAL works with a very simple description of the radiation, with only five quantities evolved in each grid cell:

the radiation energy density \hat{E} in the fluid frame, the radiation three-flux vector \vec{F} in the fluid frame, and the photon number density n_r in the radiation rest frame (Sądowski & Narayan 2015a). From the time-averaged \hat{E} , we obtain the mean bolometric radiation intensity J in the fluid frame:

$$\text{KORAL : } J = \frac{c\hat{E}}{4\pi}. \quad (11)$$

HEROIC computes the radiation field in detail, solving for the intensity $I_{\nu}(\Omega)$ in each cell over 162 ray directions Ω and 101 frequencies ν . From this we calculate J by integrating over frequency and averaging over direction:

$$\text{HEROIC : } J = \frac{1}{4\pi} \int \int I_{\nu}(\Omega) d\nu d\Omega. \quad (12)$$

Figure 2 shows the radiation and temperature solutions in the inner region of the flow ($r < 30GM/c^2$) for the fiducial model as obtained with KORAL and HEROIC. The KORAL solution for J (Top Left panel) shows an obvious thick disk plus a wide funnel, as expected for a super-Eddington accretion flow. The radiation intensity is large inside the optically thick disk, and is much less in the funnel. The radiation field shows some inhomogeneous structure, especially close to the poles. This is an artifact introduced by the M1 closure scheme in KORAL (see the discussion of the “radiation shock” effect in Sądowski et al. 2015). Although KORAL includes a radiation viscosity term to mitigate this artifact, it is unable to eliminate it altogether.

The Top Right panel in Figure 2 shows the HEROIC solution for J at the end of Stage I, i.e., using the temperature structure obtained in KORAL, but solving for the full angular and frequency structure of the radiation field. HEROIC eliminates some of the inhomogeneities in the polar radiation field. However, the HEROIC solution ends up with quite a bit more radiation in the funnel compared to the KORAL solution, especially at angles around $30^{\circ} - 40^{\circ}$ from the axis. In fact, this model produces significantly more radiation than the viscous dissipation requires and is thus much too luminosity. The reason for this can be understood as follows. Because the KORAL solution had a mild deficit of radiation near the poles, Compton-cooling was less efficient. Therefore, KORAL introduced a fairly large gas temperature in order to produce the necessary Compton-cooling to balance the viscous heating. HEROIC does not have a deficit of radiation at the poles. If we insist on using the same temperature as KORAL obtained, as is done in Stage I, then the resulting Compton-cooling is too strong and the funnel produces too much luminosity.

The above discrepancy is fixed when we solve self-consistently for the gas temperature with HEROIC so as to match the viscous heating rate. The Middle Left panel in Figure 2 shows the result we obtain after Stage III. Notice that the radiation field is smooth in the funnel, with no trace of any inhomogeneity. At the same time, the overall radiation intensity in the funnel is fairly well-matched to the KORAL result (Top Left), and much less than that of the HEROIC Stage I result (Top Right). The corresponding change in the temperature in the funnel is fairly large, as can be seen by comparing the KORAL temperatures (Bottom Left panel) and the self-consistent HEROIC temperatures (Bottom Right). The differences are primarily in the funnel, whereas the temperature in the disk interior is hardly changed.

¹ HEROIC can handle 3D data, but this was not used in the present work.

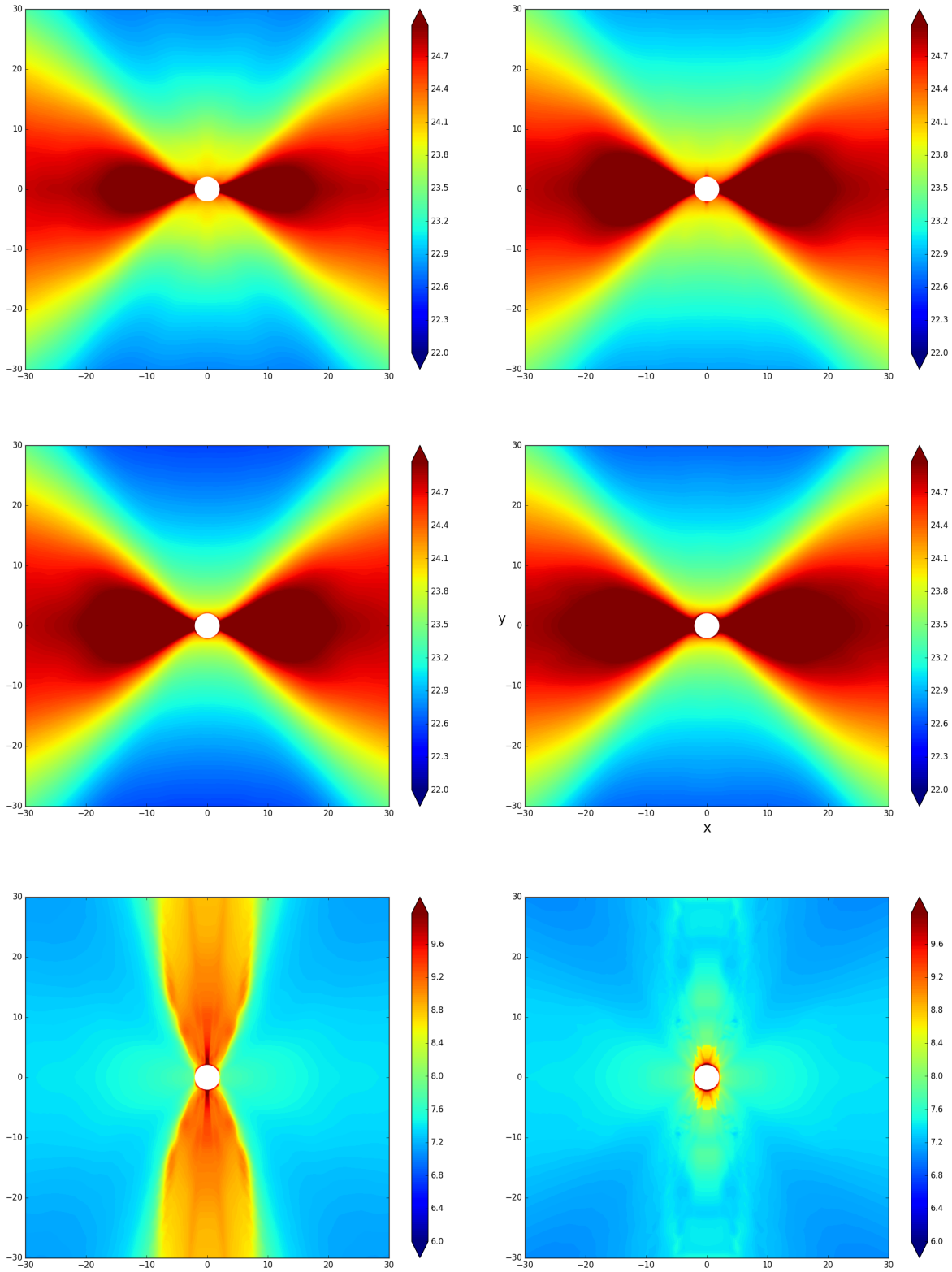


Figure 2. The top four panels show the mean bolometric radiation intensity $\log J$ as a function of position in the poloidal plane. Top Left: The distribution of $\log J$ as determined from the KORAL simulation of the fiducial model r010.3d. Top Right: HEROIC solution for J after Stage I, i.e., keeping the temperature fixed at the KORAL values and solving only for the radiation. Middle Left: HEROIC solution for J after Stage III, i.e., solving for both the temperature and the radiation field. Middle Right: Corresponding HEROIC solution after Stage III for the 2D model r010.2d. Bottom Left: Original KORAL solution for the temperature distribution ($\log T$) in the 3D model r010.3d. Bottom Right: HEROIC solution for the temperature after Stage III.

The above comparison shows that, in radiatively efficient regions of the accretion flow, it is preferable to solve for the temperature self-consistently with **HEROIC**. Because **KORAL** uses a moment method and M1 closure, it does not include enough degrees of freedom in its description of the radiation field to obtain accurate results. Presumably, a more ambitious radiation scheme, such as a general relativistic version of the variable Eddington tensor (VET) method described in [Jiang et al. \(2012\)](#), will perform better. Meanwhile, working with **KORAL**, we find that it is necessary to post-process with **HEROIC** up to Stage III, or at least Stage II, if we wish to have a consistent description of the radiation field in the funnel. The optically thick and advective regions of the flow do not require such care.

The Middle Right panel in Figure 2 shows the result we obtain after Stage III for the radiation intensity J of model r010.2d, the 2D version of the fiducial model. This **KORAL** simulation ran significantly faster than the 3D model (by a factor of tens), yet the results for the radiation field agree surprisingly well with those of the 3D model shown in the Middle Left panel (see also the comparison of spectra below). This suggests that it is generally safe to use 2D models to compute radiation quantities ([Sądowski & Narayan 2016](#)). In the rest of the paper, we freely mix results from 3D and 2D models. The one exception is the MAD models, which cannot be run in 2D.

Figure 3 is another illustration of the same results. The top two panels show profiles of the mean radiation intensity and the gas temperature as a function of polar angle θ . The different line types correspond to the original **KORAL** solution (dotted lines), the **HEROIC** result after Stage I, keeping the temperature fixed at the **KORAL** values (dashed lines), and the **HEROIC** result after Stage III, where the temperature is adjusted consistently (solid lines). The results generally confirm the previous discussion in connection with Figure 2. The jagged structure of the temperature solutions is because the viscous heating rate q^+ is patchy (Fig. 1). The effect is most severe at small radii near the BH horizon and is mostly restricted to moderately optically thick regions. It does not seem to have a strong effect on observables.

The bottom two panels in Fig. 3 compare two **HEROIC** solutions. The solid lines show the standard solution we have already described, in which the temperature is obtained self-consistently and we apply both short characteristics and long characteristics (Stage III). The dashed lines show the solution obtained via the short characteristics method alone (Stage II), i.e., without doing a final round of long characteristics. The latter shows only a small deviation from the more exact Stage III calculation. Therefore, in principle, it may be sufficient to stop after doing short characteristics, at least if we are interested only in the radiation field at small radii. The differences are more noticeable at larger radii because of the presence of ray defects in the short characteristic solution (see [Zhu et al. 2015](#)).

We also computed a **HEROIC** solution of the fiducial model in which we included thermal synchrotron radiation. The radiation field and spectrum are virtually identical to those of the solution without this emission. Thus, for the fiducial model at least, synchrotron emission is negligible. This is not surprising, since the gas temperature is below 10^9 K everywhere.

3.2 Spectra and images

Model r010.3d has a large accretion rate of $10\dot{M}_{\text{Edd}}$, so the accretion flow is expected to be geometrically thick. This is illustrated by the plots of the optical depth τ shown in Fig. 4. As we see, the optically thin funnel near the BH has an opening angle less than 30° . Note that this angle is much less than the funnel opening angle one might estimate from Figure 2. In fact, even Figure 4 is a little misleading because τ here is measured from the pole, at constant radius. If we instead computed the effective τ in the radial direction to a distant observer, the funnel would appear even narrower (as discussed later). The basic result, however, is the same, namely, only observers within a fairly small angle of the pole are able to see the intense radiation produced at the bottom of the funnel. Observers at larger radii will still receive some radiation from the walls of the funnel, plus of course emission from the disk farther out, but the hottest region at the bottom of the funnel will be invisible to them. The disk geometry thus has an obvious effect on the observed spectrum as a function of inclination angle.

Figure 5 shows spectra computed by ray-tracing (Stage IV) for observers at different inclination angles. For inclination angles of 10° and 20° , the observer sees a fairly hot spectrum that peaks at several keV and has an isotropic equivalent luminosity close to 10^{40} erg s $^{-1}$. This is fairly similar to spectra observed in ULXs.

Already at $i = 30^\circ$, the most intense radiation from the bottom of the funnel is no longer visible to the observer. The luminosity decreases, and the spectrum softens dramatically. This effect becomes more pronounced at higher inclinations. By $i = 60^\circ$, the observed luminosity is less than 10^{38} erg s $^{-1}$. Interestingly, this spectrum shows considerable resemblance to that of a “classical” supersoft source ([van den Heuvel et al. 1992](#)) or of an ultraluminous supersoft source ([Urquhart & Soria 2016](#)).

Figure 5 also shows spectra computed from model r010.2d, which is the 2D version of the fiducial model. The computed spectra are quite similar to those obtained from the 3D model, with a small mismatch in the overall luminosity. This comparison is encouraging, since 2D models are much cheaper to run than equivalent 3D models.

Figure 6 shows images computed with **HEROIC** (Stage IV) for four inclination angles. They illustrate the geometrical arguments that were used above to explain the dramatic effect of the inclination angle on observed spectra. As can be seen, only observers at inclination angles $\leq 20^\circ$ receive radiation from the hot bright region at the bottom of the funnel. Already at 30° , this region is hidden and the observed radiation is dominated by emission from the funnel wall at tens of GM/c^2 . By 40° , the observer only sees regions of the funnel wall at large radii. The observed luminosity drops rapidly and so does the spectral hardness.

4 DEPENDENCE ON PARAMETERS

4.1 Mass accretion rate

Figure 7 shows the effect of changes in the mass accretion rate. The four models have $M = 10M_\odot$, $a_* = 0$, SANE magnetic field, and $\dot{M} = 1, 7, 10, 17\dot{M}_{\text{Edd}}$, respectively. For an observer inclination angle of 10° , model r012.3d, with the

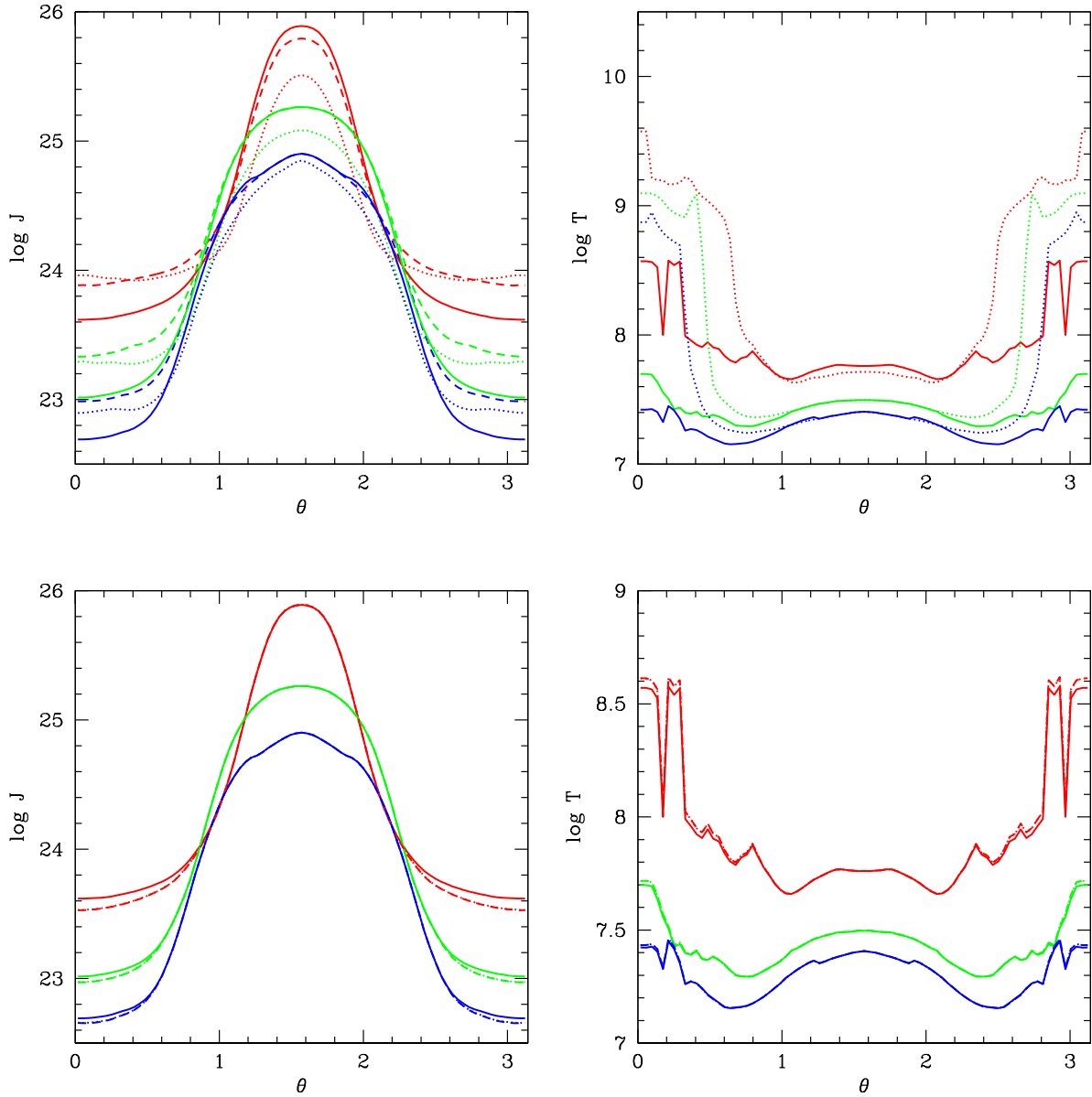


Figure 3. Top Left: Radiation intensity J in the fiducial model r010_3d as a function of Boyer-Lindquist angle θ at three Boyer-Lindquist radii: $r = 5M$ (red), $15M$ (green), $25M$ (blue). Solid lines correspond to the HEROIC solution after Stage III (see Middle Left panel in Fig. 2). Dotted lines correspond to the original solution from KORAL (Top Left, Fig. 2). Dashed lines correspond to the HEROIC solution after Stage I (Top Right, Fig. 2). Top Right: Corresponding temperature profiles vs θ at the same three radii. Bottom Left: Profiles of J in the HEROIC solution after Stage III (solid lines) and Stage II (dashed lines). Bottom Right: Corresponding temperature profiles.

lowest $\dot{M} = 1\dot{M}_{\text{Edd}}$, has a spectrum not unlike that of a thin accretion disk model. The three other models behave differently, with their spectra showing a much broader peak. In fact, these three models are quite similar to one another, both in luminosity and spectrum, which suggests that at higher \dot{M} , the observed spectrum is insensitive to the accretion rate. Curiously, model r010_3d is less luminous than

models r030_2d and r031_2d, even though its mass accretion rate lies in between the other two models. This is in part the result of a general trend we see, namely, that 3D simulations with KORAL tend to be a little less luminous than 2D models with the same parameters.

At an inclination angle of 50° , all four models in Figure 7 have substantially lower luminosity and have much softer

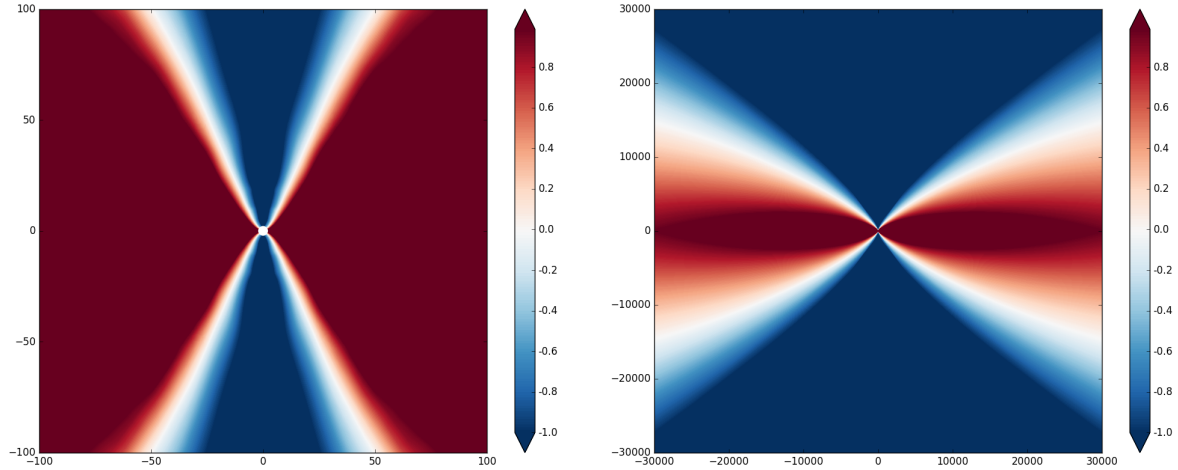


Figure 4. Shows logarithm of the electron scattering optical depth $\log \tau$ as a function of position in the poloidal plane in the fiducial model r010_3d. Red regions are optically thick, blue regions are optically thin, and the white zone corresponds to $\tau \sim 1$. The left panel shows a region close to the BH and the right panel corresponds to a larger region. The τ shown here is measured from the nearest pole.

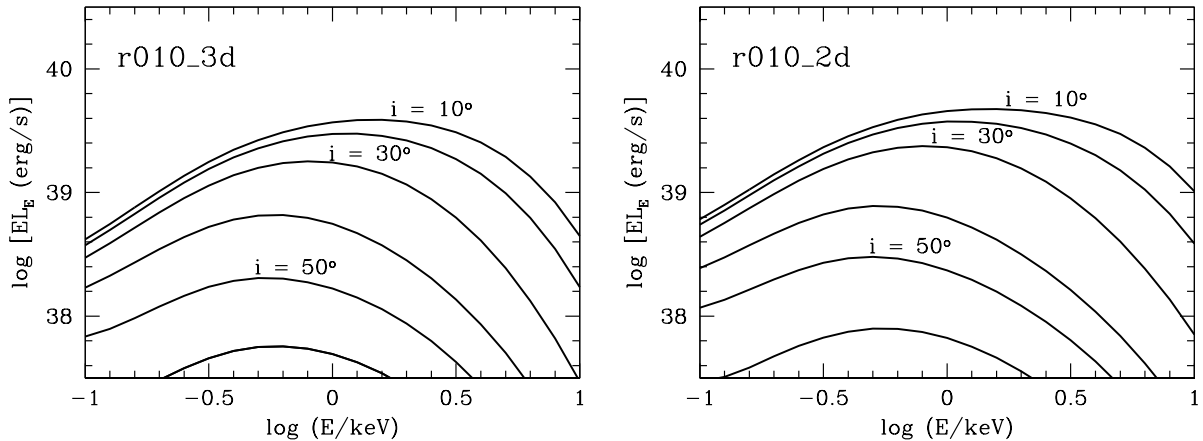


Figure 5. Left: Spectra of the fiducial model r010_3d as seen by observers at different inclination angles i . Note the rapid softening of the spectrum and the fall-off of the luminosity for inclinations of 30 deg and above. Right: Shows spectra for the 2D model r010_2d. The results are similar.

Table 2. Luminosities and efficiencies of models with $a_* = 0$

Model	\dot{M}^1	L_{rad}^2	L_{total}^2	η_{rad}	η_{total}
r010_3d/SANE	10	2.0	6.6	0.009	0.030
r010_2d/SANE	10	2.3	9.4	0.010	0.043
r012_3d/SANE	1.2	0.7	1.2	0.027	0.044
r030_2d/SANE	7.0	2.4	5.7	0.016	0.037
r031_2d/SANE	17	2.4	16	0.006	0.043
r013_3d/MAD	23	1.6	18	0.003	0.035
r023_3d/MAD	1.3	0.76	3.2	0.027	0.111

¹ In units of \dot{M}_{Edd} with $\eta_{\text{NT}} = 0.05719$

² In units of $10^{39} \text{ erg s}^{-1}$

spectra. This is because the models are sufficiently geometrically thick — even in the case of the $1\dot{M}_{\text{Edd}}$ model — that the inner region of the disk is screened from the view of the observer. Thus, the observer sees only cooler and less luminous radiation from larger radii.

While the above discussion is related to specific observer inclinations, Table 2 shows the total radiative luminosities L_{rad} of the $a_* = 0$ models integrated over all angles. These show the same pattern as a function of \dot{M} . A particularly striking result is that L_{rad} apparently saturates at roughly $2L_{\text{Edd}}$, even for quite super-Eddington accretion rates. Also

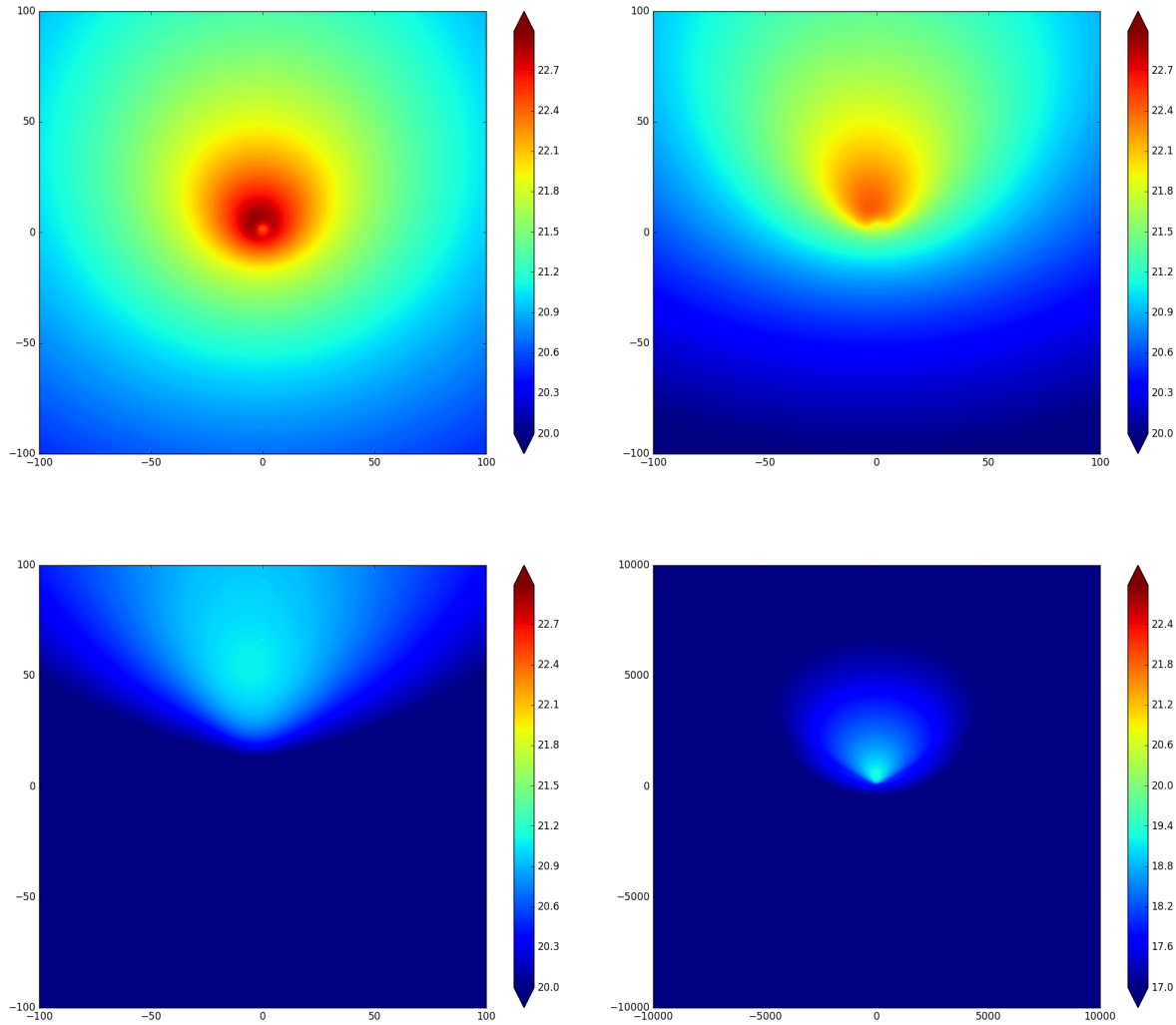


Figure 6. Top Left: Image of the fiducial model r010.3d as seen by an observer at inclination angle $i = 10$ deg from the pole. Color indicates logarithm of the brightness. Note the intense radiation emerging from near the BH, which dominates the observed radiation. Top Right: $i = 20$ deg. The bright region near the BH is still visible. Bottom Left: $i = 30$ deg. The bright region is no longer visible, and the observed radiation comes primarily from the wall of the funnel. Bottom Right: $i = 40$ deg. This is again dominated by radiation from the wall. Note that both the linear scale and the color scale have been expanded significantly in this panel.

shown in Table 2 is the radiative efficiency η_{rad} , defined as

$$\eta_{\text{rad}} \equiv \frac{L_{\text{rad}}}{\dot{M}c^2}. \quad (13)$$

The high- \dot{M} models are clearly radiatively inefficient. This is expected for the super-Eddington “slim disk” (Abramowicz et al. 1988) regime of accretion, where advection dominates.

In contrast to the radiative luminosity, the mechanical energy output of slim disks via jets and winds is not Eddington-limited. This is reflected in Table 2 in the total luminosities L_{total} (radiation+jet+wind) and the corresponding efficiencies,

$$\eta_{\text{total}} \equiv \frac{L_{\text{total}}}{\dot{M}c^2}. \quad (14)$$

Note in particular the high \dot{M} model r031.2d, which has a radiative luminosity of only 2.4×10^{39} erg s $^{-1}$ and a corre-

sponding radiative efficiency of only 0.6%, whereas its total luminosity and total efficiency are 1.6×10^{40} erg s $^{-1}$ and 4.3%.

4.2 Black hole spin

Figure 8 is similar to Figure 7, except that the models considered here have spin $a_* = 0.9$. These spectra have the same general shape as the $a_* = 0$ models. However, the spectra are noticeably harder. This suggests that it might be possible to obtain a rough estimate of the BH spin from spectral hardness. However, the method works only for observers at favorable inclination angles. For larger inclinations, the spectra are soft and are not very different from those of the $a_* = 0$ models. As in Figure 7, the spectra in Figure 8 are again insensitive to \dot{M} .

Table 3 lists the radiative and total luminosities and

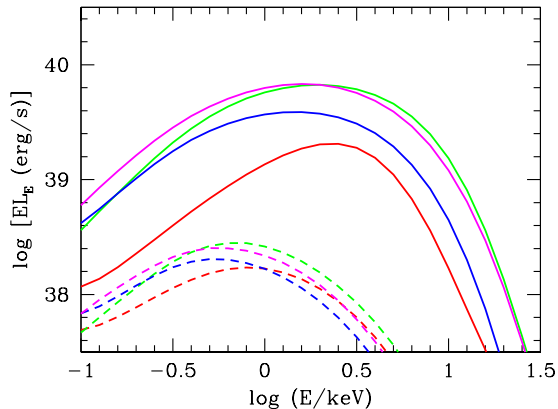


Figure 7. Spectra of models with $M = 10M_{\odot}$, $a_* = 0$, SANE magnetic field, and varying \dot{M} . Colors are as follows: $\dot{M} = 1.2\dot{M}_{\text{Edd}}$ (red, model r012_3d), $\dot{M} = 7\dot{M}_{\text{Edd}}$ (green, model r030_2d), $\dot{M} = 10\dot{M}_{\text{Edd}}$ (blue, model r010_3d), $\dot{M} = 17\dot{M}_{\text{Edd}}$ (magenta, model r031_2d). Solid lines correspond to an observer inclination angle $i = 10^\circ$, and dashed lines to $i = 50^\circ$.

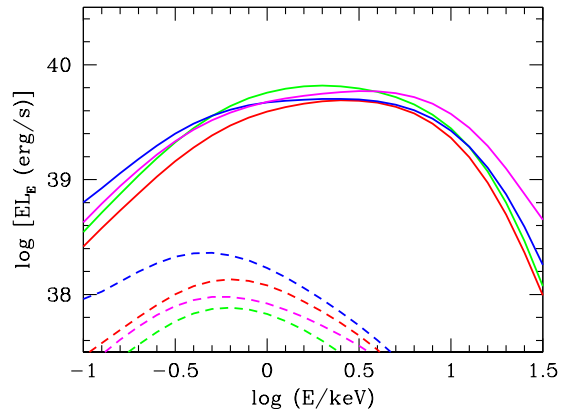


Figure 8. Spectra of models with $M = 10M_{\odot}$, $a_* = 0.9$, SANE magnetic field, and varying \dot{M} . Colors are as follows: $\dot{M} = 6.2\dot{M}_{\text{Edd}}$ (red, model r032_2d), $\dot{M} = 10\dot{M}_{\text{Edd}}$ (green, model r033_2d), $\dot{M} = 12\dot{M}_{\text{Edd}}$ (blue, model r011_2d), $\dot{M} = 26\dot{M}_{\text{Edd}}$ (magenta, model r034_2d). Solid lines correspond to an observer inclination angle $i = 10^\circ$, and dashed lines to $i = 50^\circ$.

Table 3. Luminosities and efficiencies of models with $a_* = 0.9$

Model	\dot{M}^1	L_{rad}^2	L_{total}^2	η_{rad}	η_{total}^3
r011_3d/SANE	12	2.2	9.1	0.023	0.094
r032_2d/SANE	6.2	2.0	4.3	0.039	0.087
r033_2d/SANE	10	2.5	6.6	0.031	0.082
r034_2d/SANE	26	1.7	24	0.008	0.116
r014_3d/MAD	36	57	200	0.20	0.69
r015_3d/MAD	6.8	7.2	39	0.13	0.71

¹ In units of \dot{M}_{Edd} with $\eta_{\text{NT}} = 0.1558$

² In units of $10^{39} \text{ erg s}^{-1}$

corresponding efficiencies of the $a_* = 0.9$ models. The pattern is similar to that shown by the $a_* = 0$ models. The radiative luminosity saturates at a couple of Eddington, which implies that the radiative efficiency falls substantially with increasing \dot{M} ; for instance, η_{rad} is only 0.8% for model r034_2d. In contrast, the total efficiency is around 10%, independent of \dot{M} .

4.3 MAD models

The four MAD models listed in Table 1 are all run in 3D. In these models, the magnetic field near the BH and in the inner region of the accretion disk is very strong, so much so that direct accretion via an axisymmetric disk is not possible. Gas can accrete only via non-axisymmetric streams and blobs, triggered by the interchange (or other similar) instability (Igumenshchev et al. 2003; Narayan et al. 2003; Tchekhovskoy et al. 2011; McKinney et al. 2012, 2015). Since the presence of a non-axisymmetric flow is a key feature of the MAD regime, MAD models have to be run in 3D and are quite expensive. We report results here for four MAD models.

Figure 9 shows spectra of the four models. The two models with spin 0 (Left panel) display an unusual behavior: the model with a higher $\dot{M} = 23\dot{M}_{\text{Edd}}$ has a very much softer spectrum than the one with a lower $\dot{M} = 1.3\dot{M}_{\text{Edd}}$. The reason for this unexpected behavior can be understood from Figure 10. The left two panels in the top row show the optical depth τ_{radial} as measured along the radius from infinity (this is different from the τ shown in Fig. 4). Notice that the funnel in the $23\dot{M}_{\text{Edd}}$ model is optically quite thick. This means that even observers who are perfectly aligned with the axis do not receive radiation directly from the bottom of the funnel, but rather from a photosphere at a large radius $\sim 100GM/c^2$. Correspondingly, the received radiation tends to be very soft. The $1.3\dot{M}_{\text{Edd}}$ model has less opacity in the funnel, so an aligned observer can see farther down into the funnel and observes a harder spectrum.

The above discussion is fairly specific to non-spinning (or slowly-spinning) BHs. Because of the lack of (or at best weak) frame-dragging, these systems do not have an extra power source in the BH ergosphere, as needed for the Blandford & Znajek (1977) mechanism of powering jets. The primary power source is the accretion disk. Any radiation that flows into the funnel carries some gas with it, thereby enhancing the opacity in the funnel.

The two MAD models with spin $a_* = 0.9$ are quite different. These models are substantially more luminous and also have very hard spectra (Fig. 9). The models are highly jet-dominated, as is evident from Figure 10. The jets clearly receive their power from the spinning BH via the Blandford & Znajek (1977) mechanism (which can be understood as a generalized version of the Penrose 1969 process, see Lasota et al. 2014). The funnels in these models are quite empty of gas (even in the case of the model with $\dot{M} = 36\dot{M}_{\text{Edd}}$), presumably because the gas is rapidly blown away by the

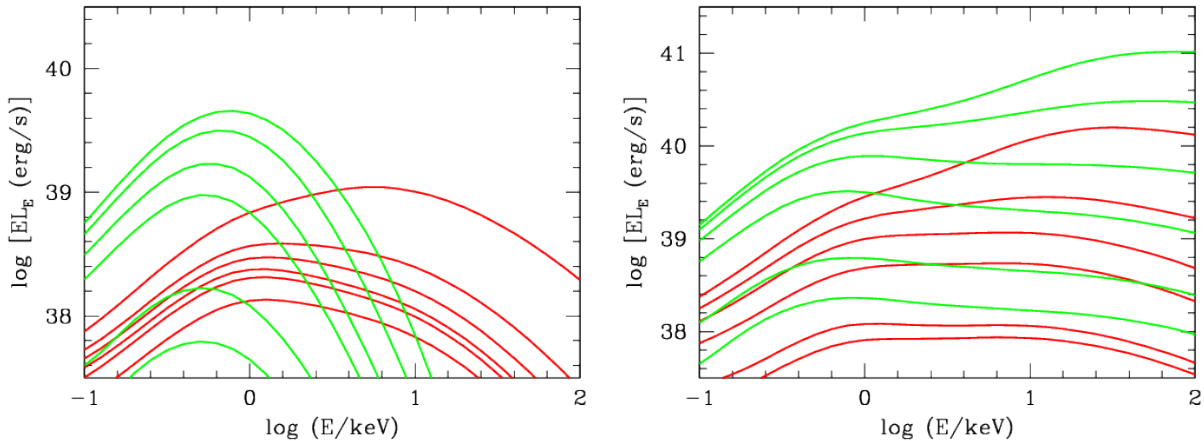


Figure 9. Left: Spectra of two MAD models with BH spin $a_* = 0$. The different-colored lines correspond to $\dot{M} = 1.3\dot{M}_{\text{Edd}}$ (red, model r023_3d) and $23\dot{M}_{\text{Edd}}$ (green, model r013_3d), respectively. For a given color, from above, the lines are for different observer inclinations: $i = 10^\circ, 20^\circ, 30^\circ, 40^\circ, 50^\circ, 60^\circ$. Right: MAD models with $a_* = 0.9$, and $\dot{M} = 6.8\dot{M}_{\text{Edd}}$ (red, model r015_3d) and $36\dot{M}_{\text{Edd}}$ (green, model r014_3d), respectively.

powerful jet. As a result, observers at low inclination angles can see down to the base of the funnel.

The lower panels in Figure 10 show the bulk Lorentz factor of the gas in the funnel for the four MAD models. The two $a_* = 0$ models have gas with only modest velocities, whereas the two $a_* = 0.9$ models show quite relativistic motions. The latter models have powerful jets driven by the BH spin. Relativistic beaming thus causes both the luminosity and the spectral hardness to be strongly enhanced. In fact, model r014_3d has an apparent luminosity $> 10^{41} \text{ erg s}^{-1}$ for an observer at inclination angle 10° , which corresponds to $> 100L_{\text{Edd}}$ for the given BH mass.

Tables 2 and 3 list the luminosities and efficiencies of the MAD models. The $a_* = 0$ MAD models have similar luminosities as their SANE counterparts. The $a_* = 0.9$ MAD models, on the other hand, are substantially more luminous than equivalent SANE models.

4.4 Dependence of Luminosity on Parameters

Figure 11 shows the apparent luminosity in the (0.3–10) keV band as a function of \dot{M} for the various model sequences. The observer is assumed to be at an inclination angle of 10° . SANE models appear to saturate in luminosity at about $2 \times 10^{40} \text{ erg s}^{-1}$ (for a BH mass of $10M_\odot$). MAD models show much more variation. Especially when the BH is spinning, MAD models can be extremely luminous.

Figure 12 plots the angle-integrated radiative luminosities L_{rad} and total luminosities L_{total} listed in Tables 2 and 3 as a function of the Eddington-scaled mass accretion rate. The values of L_{rad} are generally quite modest compared to the large apparent luminosities shown in Figure 11 for a favorably oriented observer. Figure 12 shows a striking pattern. All SANE models, as well as MAD models with a non-spinning BH, behave similarly. Their radiative luminosities

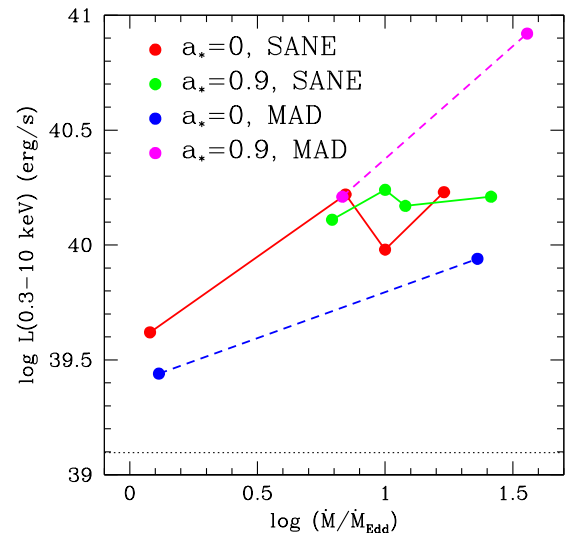


Figure 11. Apparent luminosity in the 0.3 – 10 keV band for an observer at inclination angle 10° , as a function of the mass accretion rate \dot{M} , for sequences of SANE and MAD models with BH spin values of $a_* = 0$ and 0.9 . The horizontal dotted line corresponds to the Eddington luminosity.

saturate at around $2L_{\text{Edd}}$, which means that they are radiatively inefficient at large accretion rates. Their total luminosities, however, scale roughly as $(\dot{M}/\dot{M}_{\text{Edd}})L_{\text{Edd}}$, i.e., the efficiency measured via the total luminosity is independent of the accretion rate.

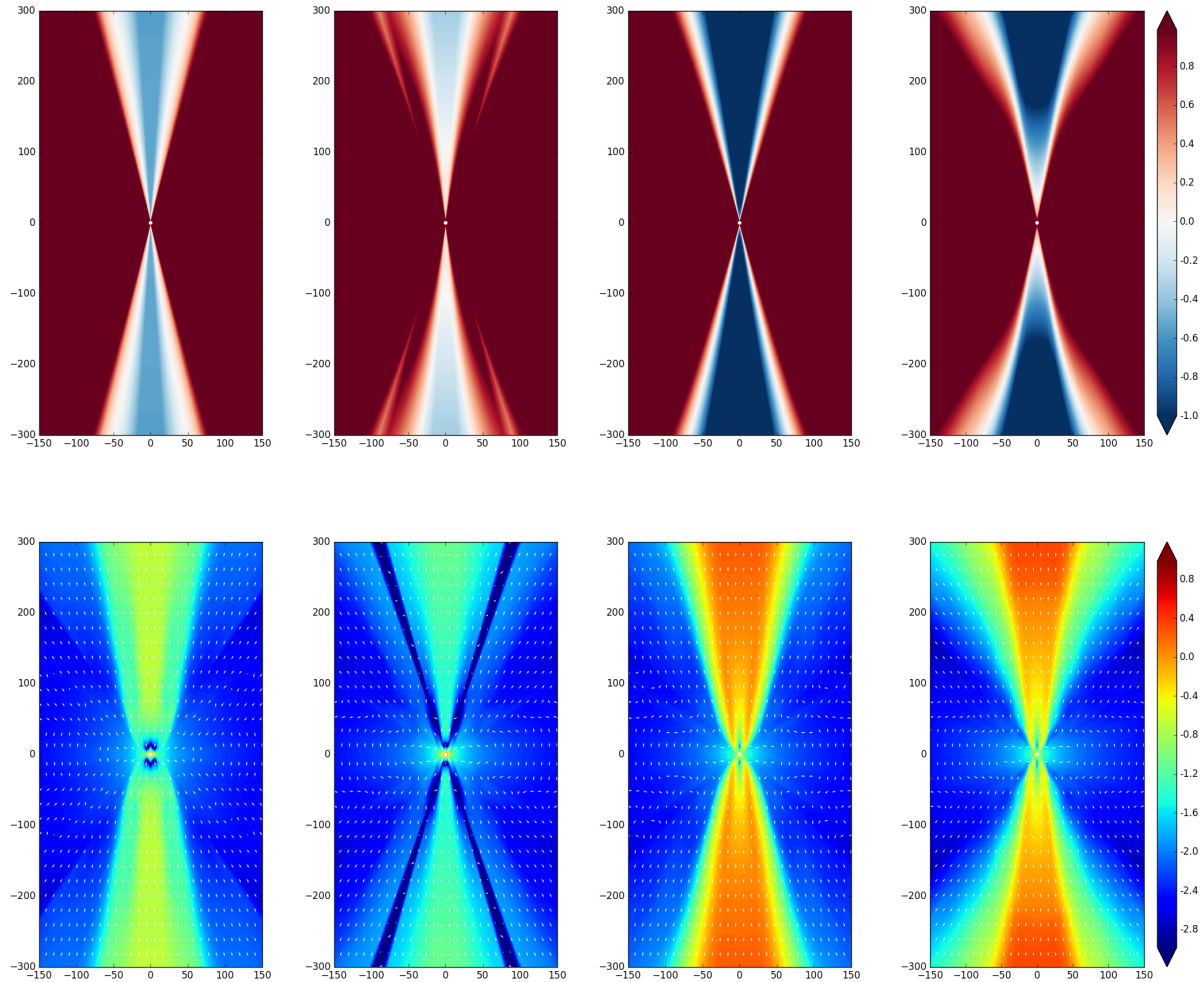


Figure 10. Top Panels: Logarithm of the optical depth $\log \tau_{\text{radial}}$ for four MAD models: Left: $a_* = 0$, $\dot{M} = 1.3\dot{M}_{\text{Edd}}$ (model r023_3d), Left Center: $a_* = 0$, $\dot{M} = 23\dot{M}_{\text{Edd}}$ (model r013_3d), Right Center: $a_* = 0.9$, $\dot{M} = 6.8\dot{M}_{\text{Edd}}$ (model r015_3d), Right: $a_* = 0.9$, $\dot{M} = 36\dot{M}_{\text{Edd}}$ (model r014_3d). Bottom Panels: Shows the quantity $(\gamma - 1)$ (color scale), where γ is the bulk Lorentz factor of the gas. The arrows indicate the direction of motion of the gas in the poloidal plane.

MAD models with a rapidly spinning BH are very different. They are radiatively quite efficient, with L_{rad} scaling as $\sim (\dot{M}/\dot{M}_{\text{Edd}})L_{\text{Edd}}$ even at large \dot{M} . Moreover, their efficiencies are larger yet by a factor of several when measured in terms of L_{total} . The distinct properties of the MAD models with rapidly spinning BHs is almost certainly related to the fact that they receive a powerful luminosity boost from the spin energy of the BH. As has been shown in recent work (Techevskoy et al. 2011; McKinney et al. 2012), energy extraction from the BH works best when the hole spins rapidly and the magnetic field strength approaches the MAD level.

5 COMPARISON WITH THE OBSERVED PROPERTIES OF ULXS

5.1 X-ray spectra

The observed X-ray spectra of ULXs show a variety of shapes, and do not neatly fit into “states”, unlike the spectra of sub-Eddington stellar-mass BHs. A popular phenomenological classification of ULX spectra includes four regimes (Sutton et al. 2013, Urquhart & Soria 2016; Soria 2011; Gladstone et al. 2009; Makishima 2007): a) “disk-like”, well fitted by non-standard multicolor disk models or slim disks, slightly broader than a standard disk-blackbody; b) “supersoft”, dominated by a thermal component with $kT < 150$ eV; c) “soft”, dominated by a power-law with photon index $\Gamma \sim 2 - 3$; d) “hard”, dominated by a power-law with $\Gamma \sim 1 - 2$. The power-law component often shows a break at a characteristic photon energy $\approx 5 - 6$ keV, a feature seen in both soft and hard ULX spectra, but not in sub-Eddington stellar-mass BHs. Also, both soft and hard ULXs

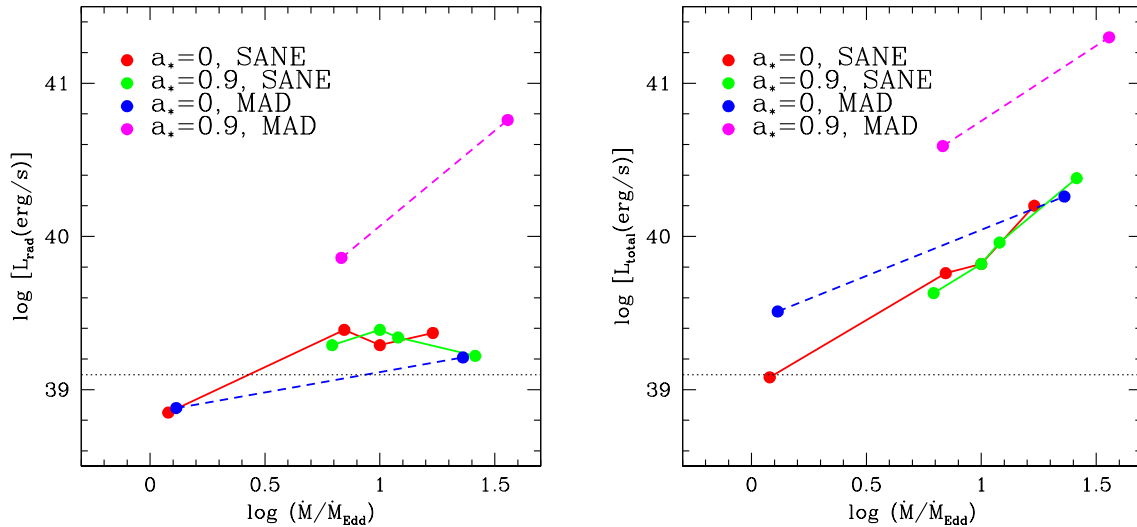


Figure 12. Total angle- and frequency-integrated radiative luminosity L_{rad} (left) and total angle-integrated net luminosity (radiation+jet+wind) L_{total} , as a function of the mass accretion rate \dot{M} , for various sequences of SANE and MAD models with BH spin values of $a_* = 0$ and 0.9. The horizontal dotted line corresponds to the Eddington luminosity.

often show an additional (non-dominant) thermal component with $kT \approx 150 - 300$ eV.

When observed at sufficiently high signal to noise, many ULXs (particularly of the supersoft and soft variety) show thermal-plasma emission lines, absorption edges and other spectral features around 1 keV (Pinto et al. 2016; Pinto et al. 2016; Urquhart & Soria 2016; Middleton et al. 2015), as expected for sources with strong outflows. It is important to stress that there is a continuum of properties between the four regimes identified above, rather than separate classes. Transitions between different ultraluminous regimes have been observed in a few cases (Sutton et al. 2013; Pintore & Zampieri 2012; Urquhart & Soria 2016); they are more frequent than transitions to and from quiescence.

The sequence of accretion states in the sub-Eddington regime of BH accretion is primarily determined by changes in the accretion rate. Here we test whether the diversity of observed spectral features in ULXs can be explained as the result of our viewing angle, because of various amounts of absorption and down-scattering of the hard X-ray photons in a dense outflow. Qualitatively, we have reproduced all four empirical regimes. For $\dot{M} \lesssim \text{few } \dot{M}_{\text{Edd}}$, we find (§4.1) that $a_* = 0$ models with a SANE magnetic field, seen at low inclination, produce a disk-like spectrum. For $\dot{M} \gtrsim \text{few } \dot{M}_{\text{Edd}}$, we find that inclination effects are much more significant than changes in the accretion rate: for $i \lesssim 30^\circ$, the shape of the observed spectrum is consistent with the hard ultraluminous regime; for $30^\circ \gtrsim i \lesssim 50^\circ$, with the soft ultraluminous regime; for $i \gtrsim 50^\circ$, with the supersoft regime (Figures 5, 7, 8).

However, this explanation is not entirely satisfactory. Our SANE models predict a steep decline in the observed luminosity as a function of viewing angle, from harder to

softer spectra: in particular, hard ULXs should appear one order of magnitude brighter than soft ULXs in the 0.3–10 keV band (Figure 5). This is inconsistent with observations, which show an overlapping distribution of hard and soft ULXs at $L_X \approx 10^{40}$ erg s $^{-1}$ (Fig. 3 in Sutton et al. 2013). In fact, there are at least two well-studied ULXs (NGC 1313 X-1 and NGC 5204 X-1) that show transitions between a soft and a hard regime, but appear brighter when softer (Sutton et al. 2013). In other cases (Holmberg II X-1: Grisé et al. 2010; Holmberg IX X-1: Luangtip et al. 2016), hardness changes appear uncorrelated with luminosity changes.

The simple fact that some ULXs show transitions between a hard and a soft regime, or between a soft and a supersoft regime (as is the case for example in M 101 ULS and NGC 247 ULS: Urquhart & Soria 2016), suggests that the viewing angle or BH spin parameter cannot be the only parameter. A variable accretion rate may play a role, perhaps also a variable magnetic field strength. For individual sources, disk precession has been invoked (Luangtip et al. 2016) to explain changes in inclination and therefore in spectral hardness, but this explanation is hard to reconcile with the short and irregular timescales seen for example in M 101 ULS (Soria & Kong 2016).

Our MAD models predict that the apparent spectral hardness depends both on viewing angle and, for a given angle, on \dot{M} , with higher accretion rates corresponding, at least for non-rotating BHs, to softer spectra and higher luminosities (Fig. 9, left panel). In this work, we have illustrated the results of MAD simulations with the rather extreme values of $a_* = 0$ and $a_* = 0.9$: we find that the low-spin models are a better approximation to ULX behaviour, with a spectral turnover between 1 and 10 keV. MAD models with $a_* = 0.9$ predict too much emission above 10 keV (regardless of accre-

tion rate and inclination), an energy band where observed ULX spectra drop much more steeply (*e.g.*, Bachetti 2016; Bachetti et al. 2013; Rana et al. 2015; Walton et al. 2014, 2013). Clearly, further work needs to be done to produce a grid of simulations over the full range of spins and mass accretion rates, but our first results are encouraging.

5.2 ULX bubbles

A powerful observational constraint we have not discussed yet is provided by the large bubbles of ionized gas seen around several ULXs (Pakull & Mirioni 2002, 2003; Pakull & Grisé 2008; Feng & Soria 2011). When such ULX bubbles are dominated by X-ray photo-ionization, the optical flux in the He II $\lambda 4686$ line provides a good proxy for the ionizing flux from the central source (Pakull & Mirioni 2002). For the photo-ionized bubble powered by the ULX in Holmberg II, the minimum input luminosity must be at least $L_X \gtrsim 4 \times 10^{39} \text{ erg s}^{-1}$ and, more likely, $L_X \gtrsim 6 \times 10^{39} \text{ erg s}^{-1}$ (Kaaret et al. 2004; Pakull & Mirioni 2002), within a factor of 2 of the apparent X-ray luminosity of this ULX (Goad et al. 2006; Sutton et al. 2013). This rules out strong beaming, at least for this source. It also shows that ULXs can have a true isotropic luminosity higher than the asymptotic upper limit ($L \approx 2.5 \times 10^{39} \text{ erg s}^{-1}$) predicted by our SANE simulations, but consistent with our MAD models at high spin (Tables 2 and 3).

Other ULXs are surrounded by shock-ionized bubbles, with diameters of $\sim 100\text{--}300$ pc, powered by a collimated jet and/or fast outflows (Pakull & Grisé 2008). The mechanical power required to inflate these bubbles is $\sim 10^{39}\text{--}10^{40} \text{ erg s}^{-1}$, consistent with the mechanical power produced in our SANE and MAD simulations (Tables 2 and 3). If the ULX photon emission were strongly beamed, we would see many shock-ionized bubbles without a strong central X-ray source for every ULX-associated bubble found. This is not what is observed: most of the large shock-ionized bubbles do contain a strong X-ray source. The number of ULX bubbles modelled in detail is still small, but the above argument (outlined in Pakull & Grisé 2008) is already a promising way to constrain the opening angle of the polar funnel in MHD simulations.

5.3 Optical counterparts

Another constraint on the accretion model and its geometry comes from the broadband emission of the optical counterpart. In X-ray binaries and ULXs, the outer region of the accretion disk intercepts and reprocesses a fraction of the X-ray flux from the central source, contributing to the broadband near-UV/optical/near-IR emission. For sub-Eddington high-mass X-ray binaries, this contribution is usually much lower than the emission from the massive donor star (Lewin et al. 1995; Frank et al. 2002). In contrast, the optical emission of low-mass X-ray binaries in outburst is dominated by the reprocessed emission of the irradiated disk (Dubus et al. 1999); there is an empirical relation (van Paradijs & McClintock 1994) between the optical luminosity of the disk, the X-ray luminosity of the central source, and the binary period (proxy for the disk size).

For a standard thin disk, theoretical models (*e.g.*,

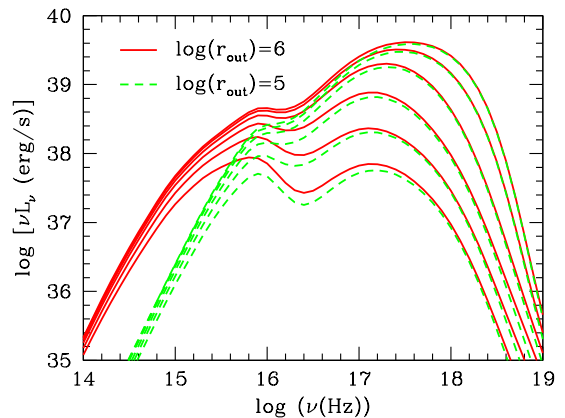


Figure 13. Broadband spectra of the fiducial model r010_3d for observers at inclination angles (from above) of 10° , 20° , 30° , 40° , 50° , 60° , respectively. The dashed green curves correspond to the case when the disk is extrapolated to $r_{\text{out}} = 10^5$ (the default) and the solid red curves correspond to $r_{\text{out}} = 10^6$.

Dubus et al. 1999; King et al. 1997; de Jong et al. 1996; Vrtilik et al. 1990) and observations (*e.g.*, Russell et al. 2014; Soria et al. 2012; Gierliński et al. 2009; Hynes et al. 2002) suggest re-emission fractions of a few times 10^{-3} . For ULXs, the relative contribution of disk and donor star is still an unsolved problem (Sutton et al. 2014; Heida et al. 2014; Gladstone et al. 2013; Grisé et al. 2012; Tao et al. 2012, 2011; Copperwheat et al. 2007). In most cases where a point-like counterpart is unequivocally identified, its near-UV/optical/near-IR luminosity is consistent both with a massive donor (usually a B-type supergiant) and with an outer accretion disk (with a size of $\sim 10^{12}$ cm) that intercepts and re-emits \sim a few $10^{37} \text{ erg s}^{-1} \sim$ a few 10^{-3} times the apparent X-ray luminosity. There is at least one ULX, the transient source in M 83 (Soria et al. 2012; Long et al. 2014), where the optical emission was proved to be from the irradiated disk, because it was only seen when the X-ray source was bright; it requires a disk reprocessing factor $\approx 5 \times 10^{-3}$.

Such high levels of disk irradiation would appear to be inconsistent with our simulated models, where the X-ray emission is strongly beamed along the polar axis. Indeed, as the broadband spectra in Figure 13 show, our fiducial model (dashed green curves) produces very little emission in the optical B-band ($\log \nu \approx 14.8$). Interestingly, when we postprocess the same model with HEROIC, but extrapolating the disk to $r_{\text{out}} = 10^6$ rather than the default $r_{\text{out}} = 10^5$, the corresponding spectra (solid red curves) have B-band luminosities surprisingly close to the levels observed in ULXs. For a $10M_\odot$ BH, $r_{\text{out}} = 10^5$ corresponds to a physical outer radius of 1.5×10^{11} cm, which is smaller than the radius $\sim 10^{12}$ cm where optical reprocessing is believed to happen.

The model with $r_{\text{out}} = 10^6$ does go out to this radius, which perhaps explains why this model agrees much better with the optical observations. One caveat is that the manner in which we extrapolate the disk to large radii is fairly approximate (§2.2), so one should not take model predictions at such radii too seriously.

6 SUMMARY AND DISCUSSION

The numerical simulations and radiative transfer calculations presented in this paper are more detailed, and include more physics, than previous work on ULXs. The closest comparison is the work of Kawashima et al. (2009, 2012), who carried out Newtonian radiation hydrodynamics simulations and post-processed their simulated models using a Monte Carlo code. The present simulations are general relativistic and include MHD, and the radiation post-processing is more sophisticated since we solve for the gas temperature. Despite these improvements, our results agree well with those of Kawashima et al. (2012)², both in the geometry of the flow (compare their Fig. 1) and in the computed spectrum as a function of observer inclination (compare their Figs. 2 – 5). Their spectra are a little harder and slightly more luminous than ours, but the qualitative agreement is striking.

We carried out a parameter study of ULX models as a function of the mass accretion rate \dot{M} , the BH spin a_* , the magnetic field strength (SANE/MAD), and the observer inclination angle i . For observers at small inclination angles (pole-on view of the disk), all the models produce super-Eddington luminosities. Even models with $\dot{M} \approx \dot{M}_{\text{Edd}}$ have X-ray (0.3 – 10 keV) luminosities of a few $\times 10^{39}$ erg s⁻¹, while models with \dot{M} equal to several \dot{M}_{Edd} have X-ray luminosities above 10^{40} erg s⁻¹ (see Fig. 11). Thus, the simulated models quite naturally produce super-Eddington apparent luminosities for suitably oriented observers. The large luminosities are caused by geometrical focusing, with a slight boost from mild relativistic beaming.

While the apparent luminosities can be large, the true angle-averaged (isotropic) radiative luminosities of the models are generally no more than $2L_{\text{Edd}}$ (see Fig. 12)³. This means that, as \dot{M} increases, the models become radiatively more and more inefficient; for example, $\eta_{\text{rad}} = 0.006$ for model r031_2d (Table 2) and 0.008 for model r034_2d (Table 3). This result is consistent with our previous work (e.g., Sądowski & Narayan 2016; Sądowski et al. 2016), but is in tension with the results reported by Jiang et al. (2014), who simulated a model with $\dot{M} = 13\dot{M}_{\text{Edd}}$ (converted to our definition of the Eddington accretion rate) and found a radiative luminosity of $10L_{\text{Edd}}$, corresponding to a radiative efficiency of 4.5%. In contrast, our model r010_3d, with $\dot{M} = 10\dot{M}_{\text{Edd}}$, has a radiative luminosity $< 2L_{\text{Edd}}$, and an efficiency of only 0.9%. To compound the problem, Jiang et al. (2014) find that a good fraction of their luminosity is

emitted inside 10 Schwarzschild radii, whereas in our models the radiation is released farther out (Sądowski et al. 2016).

The reason for the discrepancy is not clear. Jiang et al. (2014) used a Newtonian code and, because they worked with cylindrical coordinates, had a cylindrical event horizon⁴. Our code is general relativistic and models the BH horizon consistently. On the other hand, Jiang et al. (2014) used a superior method to handle radiation in their simulations, whereas our KORAL simulations use the simpler M1 closure scheme, although we then post-process the simulated model with a detailed radiative transfer computation using HEROIC. Interestingly, the discrepancy between the two codes is less severe when we consider the total luminosity: radiation+wind+jet. Jiang et al. (2014) find a total luminosity of $12L_{\text{Edd}}$ and a total efficiency $\eta_{\text{total}} = 5.4\%$, while we find for model r010_3d a total luminosity of $5.3L_{\text{Edd}}$ and $\eta_{\text{total}} = 3.0\%$. The key difference is that our GR model emits the bulk of its luminosity in a mechanical outflow whereas the Newtonian model produces mostly radiation. Perhaps the vertical advection of radiation, which Jiang et al. (2014) highlight in their work, becomes less efficient with the introduction of general relativistic dynamics in our model.

We consider next the results of our simulations in the context of ULXs. The range of spectra we find across our model parameter space includes examples that resemble all the spectral states observed in ULXs. Even the optical emission of the disk, which arises at very large radii, appears to be roughly consistent (Fig. 13). In the X-ray band, one of the key observational problems addressed in our simulations is whether the difference between softer and harder ULX spectra is primarily due to viewing angle or mass accretion rate.

We find that the spectra of models with SANE magnetic fields are essentially independent of Eddington ratio, and any softening of the spectrum is purely a result of an increasing viewing angle (Figs. 7, 8). MAD models around non-spinning BHs, by contrast, predict a dramatic spectral softening with increasing accretion rate, even for face-on observers (Fig. 9, left panel). This is caused by the optical depth of the polar outflow increasing and a scattering photosphere developing inside the funnel. A qualitatively similar softening of the observed spectrum for increasing accretion rates was also found by Kawashima et al. (2012), for similar reasons (more severe down-scattering in a denser wind); quantitatively, the softening effect is more pronounced in our zero-spin MAD models.

As a consequence of the above effect, our MAD models predict that the apparent luminosity distribution of soft ULXs should largely overlap that of hard ULXs, in agreement with observations (Sutton et al. 2013)). SANE models, on the other hand, predict that softer ULXs should always appear systematically fainter. The emergence of a photosphere in the polar funnel at very high accretion rates in the MAD models supports the suggestion of Soria & Kong (2016) (based on simple analytic approximations) that ultraluminous supersoft spectra may be caused by extremely super-Eddington accretion rates, even for low-inclination viewing angles.

There is, however, one serious problem when applying

² Note that Kawashima et al. (2012) use a different definition of \dot{M}_{Edd} : their quoted accretion rates of $200\dot{M}_{\text{Edd}}$ and $1000\dot{M}_{\text{Edd}}$ correspond to $\dot{M} \approx 11\dot{M}_{\text{Edd}}$ and $\approx 57\dot{M}_{\text{Edd}}$, respectively (for $a_* = 0$) in our definition of the Eddington accretion rate (eq. 1).

³ The discussion here does not include MAD models with spinning BHs, which are considered separately at the end of the section.

⁴ Igumenshchev et al. (2003) discuss the important role of the inner boundary condition for MHD simulations (see their Fig. 17).

our models to ULX observations. All the simulated models have geometrically thick disks with narrow funnels, requiring the observer to be located within $20 - 30^\circ$ of the poles to see the bright hard emission from gas near the BH. Off-axis observers see softer spectra with luminosities that rapidly fall below the defining luminosity limit of a ULX. The strong geometrical beaming implies that the observed ULXs should represent only $\sim 10\%$ of a larger population, the remaining $\sim 90\%$ being beamed away from us. The question then is: why have we not seen the ULX bubbles associated with these latter off-axis objects? The radiation from the bubbles should not be beamed and therefore should be visible, independent of orientation. The absence of a large population of “orphan bubbles” strongly suggests that the geometrical beaming in our simulated ULX models is too large.

There is no obvious solution to the above discrepancy. The narrow funnels in our simulations are caused by a strong radiatively-driven wind which originates close to the BH. This wind restricts the range of angles over which the hot gas near the BH is visible to a distant observer. Even models with $\dot{M} \sim 1\dot{M}_{\text{Edd}}$ (e.g., model r012_3d) show pronounced beaming, as does Fig. 1 in [Kawashima et al. \(2012\)](#). The beaming is stronger, and shows less \dot{M} dependence, than the empirical model of [King \(2009\)](#). The opening angle of the funnel is determined by the shape of the thick accretion disk at small radii. It is possible that the initial torus with which we initialize the simulations causes the disk to be too thick, and the funnel to be too narrow. It would be worthwhile to investigate how the initial conditions of the simulations affect disk thickness and degree of beaming.

A general result from this work, which should apply to all super-Eddington systems, not just ULXs, is that the angle-integrated radiative luminosity is capped at a few L_{Edd} , even when $\dot{M} \gg \dot{M}_{\text{Edd}}$, whereas the total radiative-plus-mechanical luminosity is much larger, $L_{\text{tot}} \sim (\dot{M}/\dot{M}_{\text{Edd}})L_{\text{Edd}}$ (see also [Sądowski et al. 2016](#)). Mechanical feedback should thus be very strong in super-Eddington systems. Does this feedback prevent the occurrence of super-Eddington AGN altogether? Does it prevent BH seeds from growing at super-Eddington rates in the early universe? These are open and interesting questions for future research.

We turn finally to the two models we simulated of super-Eddington MAD accretion on rapidly spinning BHs, viz., models r014_3d and r015_3d. These two models behave very differently from the other models we have discussed so far, and this regime of accretion has unique properties, as noted already by [McKinney et al. \(2014, 2015\)](#). The radiative luminosity is much higher, and the accretion is radiatively efficient even at large \dot{M} (Table 3 and Fig. 12, right panel). The spectrum is very hard and extends well above 100 keV (Fig. 9, right panel). The total luminosity, including the mechanical energy carried out in an outflow, is several times larger than the already large radiative luminosity, giving total luminosity efficiencies $\sim 70\%$ (Table 3, compare with [Tchekhovskoy et al. 2011](#), who obtained $> 100\%$ efficiency for a non-radiative MAD model). All of these unusual properties can be traced to the fact that these systems are able to use the MAD-level magnetic field to tap the spin energy of the BH, thereby producing powerful relativistic jets and strong beaming effects.

The spectra of the two large-BH-spin MAD models do not resemble the spectrum of any ULX. This suggests that

ULXs either do not reach the MAD state or do not have rapidly spinning BHs. The former possibility is unattractive since we argued earlier that slowly spinning BHs with MAD accretion do fit ULX observations; specifically, they explain luminous systems with soft spectra. Is it possible that BHs in ULXs do not have large spin values? Could the large mass accretion rate that is characteristic of the super-Eddington regime cause a rapid spin down of the holes?

Even though spinning MAD models do not appear to describe ULXs, the features they show are very promising for modeling TDE systems such as Swift J1644+57, which [Tchekhovskoy et al. \(2014\)](#) argue was produced by a spinning BH with a MAD-level magnetic field. This regime of accretion also appears promising for understanding the high energy spectra of FSRQ blazars ([Maraschi & Tavecchio 2003](#)).

7 ACKNOWLEDGEMENTS

The authors thank Magdalena Menz for help with the CHIANTI opacities used in the present work. RN was supported in part by NSF grant AST1312651, NASA grant TCAN NNX14AB47G, and the Black Hole Initiative at Harvard University, which is supported by a grant from the John Templeton Foundation. AS acknowledges support by NASA through Einstein Postdoctoral Fellowship number PF4-150126 awarded by the Chandra X-ray Center, which is operated by the Smithsonian Astrophysical Observatory for NASA under contract NAS8-03060. The authors acknowledge computational support from NSF via XSEDE resources (grant TG-AST080026N), and from NASA via the High-End Computing (HEC) Program through the NASA Advanced Supercomputing (NAS) Division at Ames Research Center. RS acknowledges hospitality at the National Astronomical Observatory of China (University of the Chinese Academy of Sciences), in Beijing, during part of this work.

REFERENCES

- Abramowicz M. A., Czerny B., Lasota J. P., Szuszkiewicz E., 1988, *ApJ*, 332, 646
- Alexander K. D., Berger E., Guillochon J., Zauderer B. A., Williams P. K. G., 2016, *ApJL*, 819, L25
- Bachetti M., 2016, *Astronomische Nachrichten*, 337, 349
- Bachetti M., Harrison F. A., Walton D. J., Grefenstette B. W., Chakrabarty D., Fürst F., Barret D., Beloborodov A., et al. 2014, *Nature*, 514, 202
- Bachetti M., Rana V., Walton D. J., Barret D., Harrison F. A., Boggs S. E., Christensen F. E., Craig W. W., et al. 2013, *ApJ*, 778, 163
- Balbus S. A., Hawley J. F., 1991, *ApJ*, 376, 214
- Balbus S. A., Hawley J. F., 1998, *Reviews of Modern Physics*, 70, 1
- Begelman M. C., King A. R., Pringle J. E., 2006, *MNRAS*, 370, 399
- Blandford R. D., Znajek R. L., 1977, *MNRAS*, 179, 433
- Castelló-Mor N., Netzer H., Kaspi S., 2016, *MNRAS*, 458, 1839
- Collin S., Kawaguchi T., 2004, *A&A*, 426, 797

- Copperwheat C., Cropper M., Soria R., Wu K., 2007, MNRAS, 376, 1407
- Coppi P. S., Blandford R. D., 1990, MNRAS, 245, 453
- Davis S. W., Narayan R., Zhu Y., Barret D., Farrell S. A., Godet O., Servillat M., Webb N. A., 2011, ApJ, 734, 111
- de Jong J. A., van Paradijs J., Augusteijn T., 1996, A&A, 314, 484
- Del Zanna G., Dere K. P., Young P. R., Landi E., Mason H. E., 2015, A&A, 582, A56
- Dere K. P., Landi E., Mason H. E., Monsignori Fossi B. C., Young P. R., 1997, A&A Suppl., 125
- Dubus G., Lasota J.-P., Hameury J.-M., Charles P., 1999, MNRAS, 303, 139
- Fabbiano G., 1989, ARAA, 27, 87
- Farrell S. A., Webb N. A., Barret D., Godet O., Rodrigues J. M., 2009, Nature, 460, 73
- Feng H., Soria R., 2011, NewAR, 55, 166
- Fragile P. C., Olejar A., Anninos P., 2014, ApJ, 796, 22
- Frank J., King A., Raine D. J., 2002, Accretion Power in Astrophysics: Third Edition
- Fürst F., Walton D. J., Harrison F. A., Stern D., Barret D., Brightman M., Fabian A. C., Grefenstette B., Madsen K. K., Middleton M. J., Miller J. M., Pottschmidt K., Ptak A., Rana V., Webb N., 2016, ApJL, 831, L14
- Fürst F., Walton D. J., Stern D., Bachetti M., Barret D., Brightman M., Harrison F. A., Rana V., 2017, ApJ, 834, 77
- Gierliński M., Done C., Page K., 2009, MNRAS, 392, 1106
- Gladstone J. C., Copperwheat C., Heinke C. O., Roberts T. P., Cartwright T. F., Levan A. J., Goad M. R., 2013, ApJS, 206, 14
- Gladstone J. C., Roberts T. P., Done C., 2009, MNRAS, 397, 1836
- Goad M. R., Roberts T. P., Reeves J. N., Uttley P., 2006, MNRAS, 365, 191
- Godet O., Barret D., Webb N. A., Farrell S. A., Gehrels N., 2009, ApJL, 705, L109
- Gould R. J., 1980, ApJ, 238, 1026
- Grisé F., Kaaret P., Corbel S., Feng H., Cseh D., Tao L., 2012, ApJ, 745, 123
- Grisé F., Kaaret P., Feng H., Kajava J. J. E., Farrell S. A., 2010, ApJL, 724, L148
- Heida M., Jonker P. G., Torres M. A. P., Kool E., Servillat M., Roberts T. P., Groot P. J., Walton D. J., Moon D.-S., Harrison F. A., 2014, MNRAS, 442, 1054
- Herold H., 1979, PRD, 19, 2868
- Hynes R. I., Haswell C. A., Chaty S., Shrader C. R., Cui W., 2002, MNRAS, 331, 169
- Igumenshchev I. V., Narayan R., Abramowicz M. A., 2003, ApJ, 592, 1042
- Israel G. L., Belfiore A., Stella L., Esposito P., Casella P., De Luca A., Marelli M., Papitto A., et al. 2016, ArXiv e-prints
- Israel G. L., Papitto A., Esposito P., Stella L., Zampieri L., Belfiore A., Rodríguez Castillo G. A., De Luca A., et al. 2017, MNRAS, 466, L48
- Jiang Y.-F., Stone J. M., Davis S. W., 2012, ApJS, 199, 14
- Jiang Y.-F., Stone J. M., Davis S. W., 2014, ApJ, 796, 106
- Jin C., Done C., Ward M., 2016, MNRAS, 455, 691
- Jones F. C., 1968, Physical Review, 167, 1159
- Kaaret P., Ward M. J., Zezas A., 2004, MNRAS, 351, L83
- Kawakatu N., Ohsuga K., 2011, MNRAS, 417, 2562
- Kawashima T., Ohsuga K., Mineshige S., Heinzeller D., Takabe H., Matsumoto R., 2009, PASJ, 61, 769
- Kawashima T., Ohsuga K., Mineshige S., Yoshida T., Heinzeller D., Matsumoto R., 2012, ApJ, 752, 18
- Kelly B. C., Shen Y., 2013, ApJ, 764, 45
- King A., 2003, ApJL, 596, L27
- King A., Lasota J.-P., 2016, MNRAS, 458, L10
- King A. R., 2009, MNRAS, 393, L41
- King A. R., Davies M. B., Ward M. J., Fabbiano G., Elvis M., 2001, ApJL, 552, L109
- King A. R., Kolb U., Szuszkiewicz E., 1997, ApJ, 488, 89
- Landi E., Young P. R., Dere K. P., Del Zanna G., Mason H. E., 2013, ApJ, 763, 86
- Lasota J.-P., Gourgoulhon E., Abramowicz M., Tchekhovskoy A., Narayan R., 2014, PRD, 89, 024041
- Levermore C. D., 1984, J Quant. Spectrosc. Radiative Transfer, 31, 149
- Lewin W. H. G., van Paradijs J., van den Heuvel E. P. J., 1995, Cambridge Astrophysics Series, 26
- Lodato G., Rossi E. M., 2011, MNRAS, 410, 359
- Long K. S., Kuntz K. D., Blair W. P., Godfrey L., Plucinsky P. P., Soria R., Stockdale C., Winkler P. F., 2014, ApJS, 212, 21
- Luangtip W., Roberts T. P., Done C., 2016, MNRAS, 460, 4417
- Lupi A., Haardt F., Dotti M., Fiacconi D., Mayer L., Madau P., 2016, MNRAS, 456, 2993
- Madau P., Haardt F., Dotti M., 2014, ApJL, 784, L38
- Mahadevan R., Narayan R., Yi I., 1996, ApJ, 465, 327
- Makishima K., 2007, in Karas V., Matt G., eds, Black Holes from Stars to Galaxies – Across the Range of Masses Vol. 238 of IAU Symposium, Observational evidence for intermediate-mass black holes: ultra-luminous X-ray sources. pp 209–218
- Makishima K., Kubota A., Mizuno T., Ohnishi T., Tashiro M., Aruga Y., Asai K., Dotani T., et al. 2000, ApJ, 535, 632
- Maraschi L., Tavecchio F., 2003, ApJ, 593, 667
- McKinney J. C., Chluba J., Wielgus M., Narayan R., Sądowski A., 2016, ArXiv e-prints
- McKinney J. C., Dai L., Avara M. J., 2015, MNRAS, 454, L6
- McKinney J. C., Tchekhovskoy A., Blandford R. D., 2012, MNRAS, 423, 3083
- McKinney J. C., Tchekhovskoy A., Sądowski A., Narayan R., 2014, MNRAS, 441, 3177
- Middleton M. J., Walton D. J., Fabian A., Roberts T. P., Heil L., Pinto C., Anderson G., Sutton A., 2015, MNRAS, 454, 3134
- Miller M. C., Colbert E. J. M., 2004, International Journal of Modern Physics D, 13, 1
- Mortlock D. J., Warren S. J., Venemans B. P., Patel M., Hewett P. C., McMahon R. G., Simpson C., Theuns T., González-Solares E. A., Adamson A., Dye S., Hambly N. C., Hirst P., Irwin M. J., Kuiper E., Lawrence A., Röttgering H. J. A., 2011, Nature, 474, 616
- Narayan R., Igumenshchev I. V., Abramowicz M. A., 2003, PASJ, 55, L69
- Narayan R., Sądowski A., Penna R. F., Kulkarni A. K., 2012, MNRAS, 426, 3241
- Narayan R., Yi I., 1995, ApJ, 452, 710

- Narayan R., Zhu Y., Psaltis D., Sądowski A., 2016, *MNRAS*, 457, 608
- Novikov I. D., Thorne K. S., 1973, in Dewitt C., Dewitt B. S., eds, *Black Holes (Les Astres Occlus) Astrophysics of black holes.* pp 343–450
- Ohsuga K., Mineshige S., 2011, *ApJ*, 736, 2
- Ohsuga K., Mori M., Nakamoto T., Mineshige S., 2005, *ApJ*, 628, 368
- Paczyński B., Wiita P. J., 1980, *A&A*, 88, 23
- Page M. J., Simpson C., Mortlock D. J., Warren S. J., Hewett P. C., Venemans B. P., McMahon R. G., 2014, *MNRAS*, 440, L91
- Pakull M. W., Grisé F., 2008, in Bandyopadhyay R. M., Wachter S., Gelino D., Gelino C. R., eds, *A Population Explosion: The Nature & Evolution of X-ray Binaries in Diverse Environments Vol. 1010 of American Institute of Physics Conference Series, Ultraluminous X-ray Sources: Beambags and Optical Counterparts.* pp 303–307
- Pakull M. W., Mirioni L., 2002, *ArXiv Astrophysics e-prints*
- Pakull M. W., Mirioni L., 2003, in Arthur J., Henney W. J., eds, *Revista Mexicana de Astronomia y Astrofisica Conference Series Vol. 15 of Revista Mexicana de Astronomia y Astrofisica, vol. 27, Bubble Nebulae around Ultraluminous X-Ray Sources.* pp 197–199
- Penrose R., 1969, *Nuovo Cimento Rivista Serie*, 1
- Pinto C., Fabian A., Middleton M., Walton D., 2016, *ArXiv e-prints*
- Pinto C., Middleton M. J., Fabian A. C., 2016, *Nature*, 533, 64
- Pintore F., Zampieri L., 2012, *MNRAS*, 420, 1107
- Poutanen J., Lipunova G., Fabrika S., Butkevich A. G., Abolmasov P., 2007, *MNRAS*, 377, 1187
- Rana V., Harrison F. A., Bachetti M., Walton D. J., Furst F., Barret D., Miller J. M., Fabian A. C., Boggs S. E., Christensen F. C., Craig W. W., Grefenstette B. W., Hailey C. J., Madsen K. K., Ptak A. F., Stern D., Webb N. A., Zhang W. W., 2015, *ApJ*, 799, 121
- Rees M. J., 1988, *Nature*, 333, 523
- Russell T. D., Soria R., Motch C., Pakull M. W., Torres M. A. P., Curran P. A., Jonker P. G., Miller-Jones J. C. A., 2014, *MNRAS*, 439, 1381
- Sądowski A., Wielgus M., Narayan R., Abarca D., McKinney J. C., Chael A., 2016a, *ArXiv e-prints*
- Sądowski A., Wielgus M., Narayan R., Abarca D., McKinney J. C., Chael A., 2016b, *ArXiv e-prints*
- Sądowski A., Lasota J.-P., Abramowicz M. A., Narayan R., 2016, *MNRAS*, 456, 3915
- Sądowski A., Narayan R., 2015a, *MNRAS*, 454, 2372
- Sądowski A., Narayan R., 2015b, *MNRAS*, 453, 3213
- Sądowski A., Narayan R., 2016, *MNRAS*, 456, 3929
- Sądowski A., Narayan R., McKinney J. C., Tchekhovskoy A., 2014, *MNRAS*, 439, 503
- Sądowski A., Narayan R., Tchekhovskoy A., Abarca D., Zhu Y., McKinney J. C., 2015, *MNRAS*, 447, 49
- Sądowski A., Narayan R., Tchekhovskoy A., Zhu Y., 2013, *MNRAS*, 429, 3533
- Shakura N. I., Sunyaev R. A., 1973, *A&A*, 24, 337
- Socrates A., 2012, *ApJL*, 756, L1
- Soria R., 2011, *Astronomische Nachrichten*, 332, 330
- Soria R., Kong A., 2016, *MNRAS*, 456, 1837
- Soria R., Kuntz K. D., Winkler P. F., Blair W. P., Long K. S., Plucinsky P. P., Whitmore B. C., 2012, *ApJ*, 750, 152
- Sutton A. D., Done C., Roberts T. P., 2014, *MNRAS*, 444, 2415
- Sutton A. D., Roberts T. P., Middleton M. J., 2013, *MNRAS*, 435, 1758
- Swartz D. A., Ghosh K. K., Tennant A. F., Wu K., 2004, *ApJS*, 154, 519
- Takahashi H. R., Ohsuga K., 2015, *PASJ*, 67, 60
- Takahashi H. R., Ohsuga K., Kawashima T., Sekiguchi Y., 2016, *ApJ*, 826, 23
- Tao L., Feng H., Grisé F., Kaaret P., 2011, *ApJ*, 737, 81
- Tao L., Kaaret P., Feng H., Grisé F., 2012, *ApJ*, 750, 110
- Tchekhovskoy A., Metzger B. D., Giannios D., Kelley L. Z., 2014, *MNRAS*, 437, 2744
- Tchekhovskoy A., Narayan R., McKinney J. C., 2011, *MNRAS*, 418, L79
- Urquhart R., Soria R., 2016, *MNRAS*, 456, 1859
- van den Heuvel E. P. J., Bhattacharya D., Nomoto K., Rappaport S. A., 1992, *A&A*, 262, 97
- van Paradijs J., McClintock J. E., 1994, *A&A*, 290, 133
- Volonteri M., Rees M. J., 2005, *ApJ*, 633, 624
- Volonteri M., Silk J., Dubus G., 2015, *ApJ*, 804, 148
- Vrtilek S. D., Raymond J. C., Garcia M. R., Verbunt F., Hasinger G., Kurster M., 1990, *A&A*, 235, 162
- Walton D. J., Fuerst F., Harrison F., Stern D., Bachetti M., Barret D., Bauer F., Boggs S. E., Christensen F. E., Craig W. W., Fabian A. C., Grefenstette B. W., Hailey C. J., Madsen K. K., Miller J. M., Ptak A., Rana V., Webb N. A., Zhang W. W., 2013, *ApJ*, 779, 148
- Walton D. J., Harrison F. A., Grefenstette B. W., Miller J. M., Bachetti M., Barret D., Boggs S. E., Christensen F. E., Craig W. W., Fabian A. C., Fuerst F., Hailey C. J., Madsen K. K., Parker M. L., Ptak A., Rana V., Stern D., Webb N., Zhang W. W., 2014, *ApJ*, 793, 21
- Wang F., Wu X.-B., Fan X., Yang J., Cai Z., Yi W., Zuo W., Wang R., McGreer I. D., Ho L. C., Kim M., Yang Q., Bian F., Jiang L., 2015, *ApJL*, 807, L9
- Watarai K.-y., Mizuno T., Mineshige S., 2001, *ApJL*, 549, L77
- Wu X.-B., Wang F., Fan X., Yi W., Zuo W., Bian F., Jiang L., McGreer I. D., Wang R., Yang J., Yang Q., Thompson D., Beletsky Y., 2015, *Nature*, 518, 512
- Zauderer B. A., Berger E., Soderberg A. M., Loeb A., Narayan R., Frail D. A., Petitpas G. R., Brunthaler A., et al. 2011, *Nature*, 476, 425
- Zhu Y., Narayan R., Sądowski A., Psaltis D., 2015, *MNRAS*, 451, 1661
- Zubovas K., King A., 2013, *ApJ*, 769, 51
- Zuo W., Wu X.-B., Fan X., Green R., Wang R., Bian F., 2015, *ApJ*, 799, 189